Electronic Supplementary Material

Heteroatoms Dual Doped Porous Graphene Nanosheets as Efficient Bifunctional Metal-Free Electrocatalysts for Overall Water-Splitting

Xin Yue,[a, b] Shangli Huang,[b] Junjie Cai,[c] Yanshuo Jin[a] and Pei Kang Shen [a, b] *

[a] School of Materials Science and Engineering, Sun Yat-sen University, Guangzhou, 510275, P. R. China.

[b] Collaborative Innovation Center of Sustainable Energy Materials, Guangxi University, Nanning 530004, P. R. China.

[c] Department of Mechanical and Biomedical Engineering, City University of Hong Kong, 83 Tat Chee Avenue, Hong Kong.

* pkshen@gxu.edu.cn (P.K. Shen)

Experimental

Synthesis

Synthesis of nitrogen and fluorine dual doped porous graphene like nanosheets (denoted as NFPGNS), nitrogen doped nanographite (denoted as NNG) and fluorine doped porous graphitized carbon (denoted as FPGC).

The NFPGNS was synthesized by a ion adsorption method: macroreticular weak basic styrene type anion exchange resin (10 g, D301, AR, > 99%, Shanghai Hualing Co. Ltd., China) was firstly adsorbed with sodium hexanitrocobaltate (0.10 M $Na_3Co(NO_2)_6$, Aladding Chemistry Co. Ltd., China) and potassium fluoride dihydrate (0.09 M (mass ratio of KF to resin to 0.5), 0.17 M (mass ratio of KF to resin to 1) and 0.26 M (mass ratio of KF to resin to 1.5), KF. $2H_2O$, Aladding Chemistry Co. Ltd., China) solution (1000 mL). Then, solution complex was sintered at 80 ^oC to removing the solvent. The resulting resin complex was then sintered at 1000 ^oC for 2 h under a pure N_2 flow. D301 anion exchange resin (10 g) was adsorbed with 0.10 M $Na_3Co(NO_2)_6$, without KF in the same condition and finally sintered at 1000 ^oC for 2 h under a pure N_2 flow to prepare NNG. Commercial carbon (10 g, Vulcan XC 72R) was adsorbed with 0.17 M KF. $2H_2O$ in the same condition and finally sintered at 1000 ^oC for 2 h under a pure N_2 flow to prepare FPGC. After slowly cooling down to room temperature, the product was ground and treated with 1 mol L^{-1} HCl solution to remove cobalt and other impurities. After washing in deionized water and drying, NFPGNS, NNG and FPGC catalysts were stored for further characterizations.

Characterizations

The X-ray diffraction (XRD) measurements were carried out on a D/Max-IIIA (Rigaku Co., Japan) employing Cu Kα (λ= 0.15406 nm) as the radiation source at 40 kV and 40 mA with a scanning rate of 10° min^{-1}. The content of Co was performed by Inductively Coupled Plasma-atomic Emission Spectrometry (ICP) on a TJA IRIS(HR). The morphologies of the samples were observed by Scanning Electron Microscopy (SEM, FEI/OXFORD/HKL, Quanta 400 FEG) Transmission Electron Microscopy (TEM, FEI Tecnai G2 F30 operating at 300 kV) investigations. Raman analysis was performed on a micro-Raman spectrometer (Renishaw inVia, U.K.). The X-ray photoelectron spectroscopy (XPS) measurements were carried out on a XPS apparatus (ESCALAB 250, Thermo-VG Scientific Ltd.). The thermal gravimetric (TG) analysis was carried out on Thermogravimetry coupled with Fourier transform infrared spectrometry (NETZSCH-

Feinmahltechnik GmbH, Selb).

Electrochemical measurements:

The electrochemical measurement was used a Bio-Logic VMP3 potentiostat with a glassy carbon electrode (Φ = 5 mm) as the working electrode, a graphite rod as the counter electrode and a reversible hydrogen electrode (RHE) electrode as the reference electrode. A two-electrode-system was used for electrochemical measurement of overall water splitting used a Bio-Logic VMP3 potentiostat with two glassy carbon electrode (Φ = 5 mm) as the working electrode. The NFPGNS, NNG, FPGC and CC (10.0 mg) and commercial Pt/C (46.7%, 4.3 mg) catalysts catalysts were dispersed in 1.5 mL ethanol and 0.5 mL Nafion (0.5 wt%, DuPont, USA) solution, respectively. The resulting mixture were then ultrasonicated for 45 min until obtain a well dispersed ink. Electrocatalysts ink was transferred to the surface of the work electrode. Then, to obtain an electrocatalysts thin film on electrode, the work electrode was dried under infrared lamp. The loadings of metal free electrocatalysts on work electrode id 2.55 mg cm^{-2}, and that of Pt/C electrocatalysts is 2.55×10^{-2} mg cm^{-2}. The electrochemical tests were performed in 1 M KOH solution at 25 ^{o}C.

DFT calculation:

DFT calculations were performed on the Dmol^3 program package (Material studio8.0, Accelrys Company) [S1, S2]. The exchanged and correlated interaction were presented by generalized gradient approximation (GGA) with Perdew-Burlce-Ernzerhof (PBE) function. DFT-D2 with a Grimme vdW method [S2] was adopted to describe corrected van der Waals interaction due to the fact that GGA/PBE was failed to describe nonlocal dispersion force. Spin-polarized was unrestricted for all calculations. Double numerical plus polarization (DNP) basis set was employed and its accuracies equaled to

Pope's 6-31G** basis set. Model of 4×4 graphene hexagonal supercell was located in a rhombus periodic box with a lattice constant a=b=30 Å, c=25 Å. The edge carbon atom dangling bond was saturated by hydrogen atom. Six models of graphene and doped graphene (pyN, F-G, pyN-G, gN, F-G, gN-G, F-G and G) were selected to modulate HER and OER. The *k*-point sampling of Brillouin zone was obtained with a 5×5×1 grid mesh using Monkhorst-Pack method [S3], and a 21×21×1 *k*-point grid was used for electric structure calculation. The convergence criterion of energy lower than 10^{-5} Ha, 0.002 Ha/Å of maximum force, and 0.005 Å of maximum displacement were used for all structure geometry optimization. The real-space global orbit cutoff radius was set to 4.7 Å in all calculations to ensure a high quality results. In order to get each reactions of rate limiting step,

Gibbs free energy was calculated (ΔG) by following equation [S4],

$\Delta G = \Delta E + \Delta E_{ZPE} - T\Delta S$

Where ΔE is directly determined by analyzing total energy as above described. T is system temperature (298.15K, in this work). ΔE_{ZPE} is difference between the adsorbed state and gas phase, and it calculated by summing vibrational frequency for all norm model. The change entropy (ΔS) is defined as difference between the adsorbed state and gas phase. The entropies of free molecular are obtained from NIST database [S5].

In this work, we assume that the OER is processed in following four electron pathway [S6]:

$OH^- + * = OH^* + e^-$ (1)

$OH^* + OH^- = O^* + H_2O + e^-$ (2)

$OH^- + O^* = OOH^* + e^-$ (3)

$OH^- + OOH^* = O_2 + H_2O + e^-$ (4)

Thus, ΔG of OH*, O* and OOH* was calculated as reasonable descriptor of OER activity for various electrocatalysts.

Meanwhile, the HER in a base proceeds in the following sequence of Volmer–Heyrovsky or Volmer–Tafel mechanisms [S7]:

Volmer: $H_2O + * + e^- = H* + OH^-$ (5)

Heyrovsky: $H* + H_2O + e^- = H_2 + OH^- + *$ (6)

Tafel: $2\ H* = H_2 + 2\ *$ (7)

In the above elementary reaction steps, adsorbed hydrogen (H*) appears to be the only reaction intermediate on the electrode surface, similar to the case in the acidic electrolyte. Therefore, ΔG of H* was calculated as reasonable descriptor of HER activity for various electrocatalysts. [7]

Synthesis processes of NFPGNS and NNG were studied by thermal gravimetric (TG) analysis. TG curves of resin-$Na_3Co(NO_2)_6$-KF and resin-$Na_3Co(NO_2)_6$ sintered in pure N_2 atmosphere were shown in Fig. S1a. In the case of NNG synthesis process, a dehydration process was undergone from room temperature to ~ 300 °C. Then, from ~ 300 °C to 500 °C, there was a carbonization process with a decomposition process, shown a strong mass loss. After ~ 500 °C, mass loss becoming very little, correspond to a graphitization process. However, in the case of NFPGNS synthesis process, after carbonization process at ~ 600 °C, there is a much stronger mass loss process than before. It indicates that the activation process by KF was occurred synchronously with the graphitization process catalyzed by Co due to the etching of carbon leading to a violent mass loss. TG analysis also investigated to prove the residue Co in tn NFPGNS and NG electrocatalysts (Fig. S1b). Results imply that after sintered under air atmosphere until 900 °C with a heating rate of 5 °C/min, the residue of this two samples were almost zero.

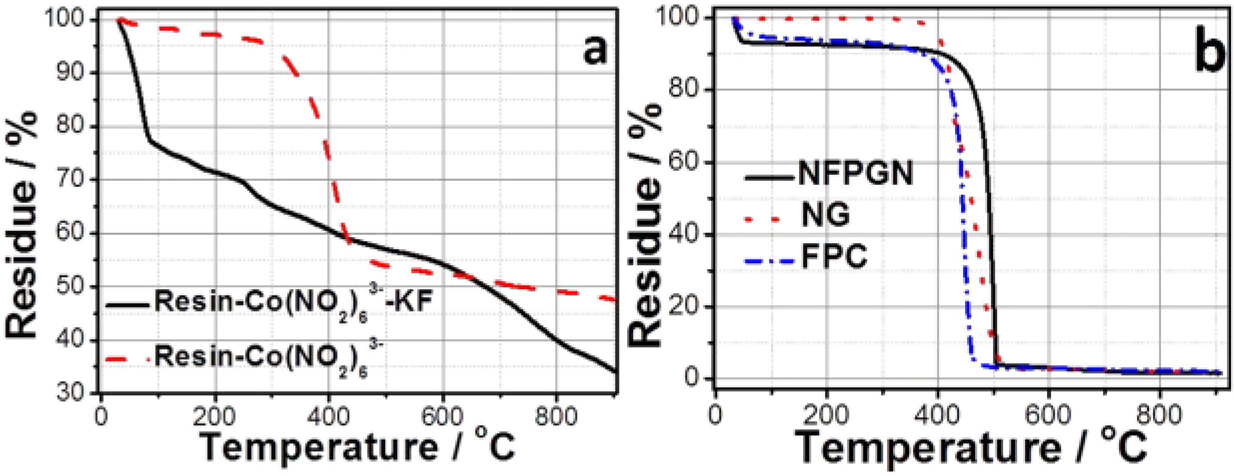

Fig. S1 (a) TG curves of resin-Na$_3$Co(NO$_2$)$_6$-KF and resin-Na$_3$Co(NO$_2$)$_6$ sintered in pure N$_2$ atmosphere with heating rate of 5 ^{o}C/min. (b) TG curves of NFPGNS, and NNG in air with heating rate of 5 ^{o}C/min.

The XRD patterns of NFPGNS and NNG sintered at different temperature are shown in the Fig. S2a and b. The graphite (002) peak occurred from temperature of 800 ^{o}C, is higher than that of NNG. This is because the loss of graphitization at the activation process by KF. However, with the temperature increased, the degree of graphitization on NFPGNS becomes higher. The XRD patterns showed a high degree of graphitization on CC and FPGC (Fig. S2c). However, the graphite (002) peak appeared at ~ 24.6 ^{o}, conforming to the results in the literature [S8].

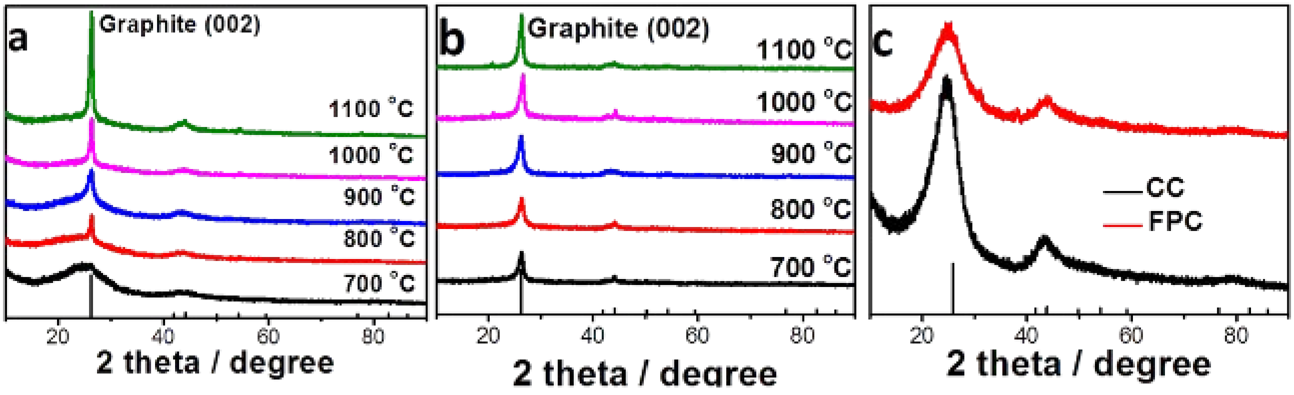

Fig. S2 XRD patterns of (a) NFPGNS sintered at different temperature, (b) NNG sintered at different temperature, and (c) CC and FPGC.

Inductively Coupled Plasma-atomic Emission Spectrometry (ICP) was performed to explore the content of Co in NFPGNS and NNG. Firstly, 10 g NFPGNS and NNG were put into corundum boat, respectively and sinter at 950 ^{o}C under air atmosphere for 2 h. The corundum boats after burning were leached in 100 mL aqua regia, respectively, and then the solution were detected by ICP. Results showed that residue Co was 0.019 and 0.184 mg/L in the detected solution, calculated to 0.019 mg in 100 g MFPGNS and 0.184 mg in 100 g NNG, respectively. Obviously, the amounts of Co in NFPGNS and NNG were very little.

Table S1 Residue Co in NFPGNS and NNG detected by ICP.

Sample	Co mg/ 100 g
NFPGN	0.019
NNG	0.184

The TEM images of NNG were shown in the Fig. S3. The morphology of NNG presented as graphite nanoparticles with average size about 50 nm. A typical high resolution TEM image was shown in the Fig. S3b. Very thick graphite layers of NNG were shown in the image without activation by chemical active agents. Therefore, N doped graphite carbon was denoted as NNG (N doped nano-graphite).

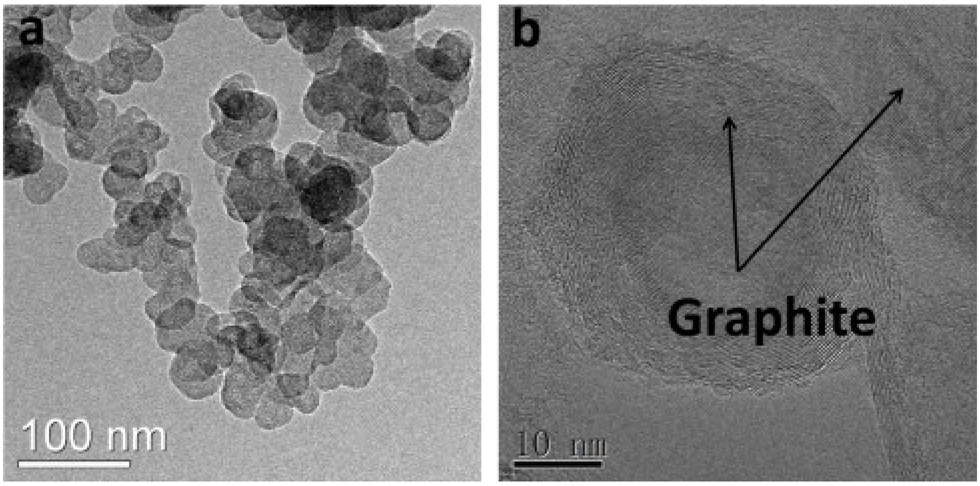

Fig. S3 The TEM images of NNG.

The TEM images of samples with different mass ratio of resin to KF are shown in Fig. S4. All of this samples were sintered at 1000 ^{o}C under pure N_2 atmosphere. In the case of lower mass ratio of KF to resin (0.5:1), few layers graphite (over 20 layers) were observed. However, increasing the mass ratio of KF to resin of 1.5:1, nanocrystalline graphite was arisen. This means that graphite structures were etched by KF in the activation process. Thick layers of graphite were produced in the case of lower amount of KF adsorbed in resin complexes. However, nanocrystaline graphite was produced by etching graphitization carbon structure with destroyed structure of graphene when a high level of KF was given. Therefore, appropriate amount of KF adsorbed on resin (resin : KF = 1:1) in the process of grapheme like structure preparation is required.

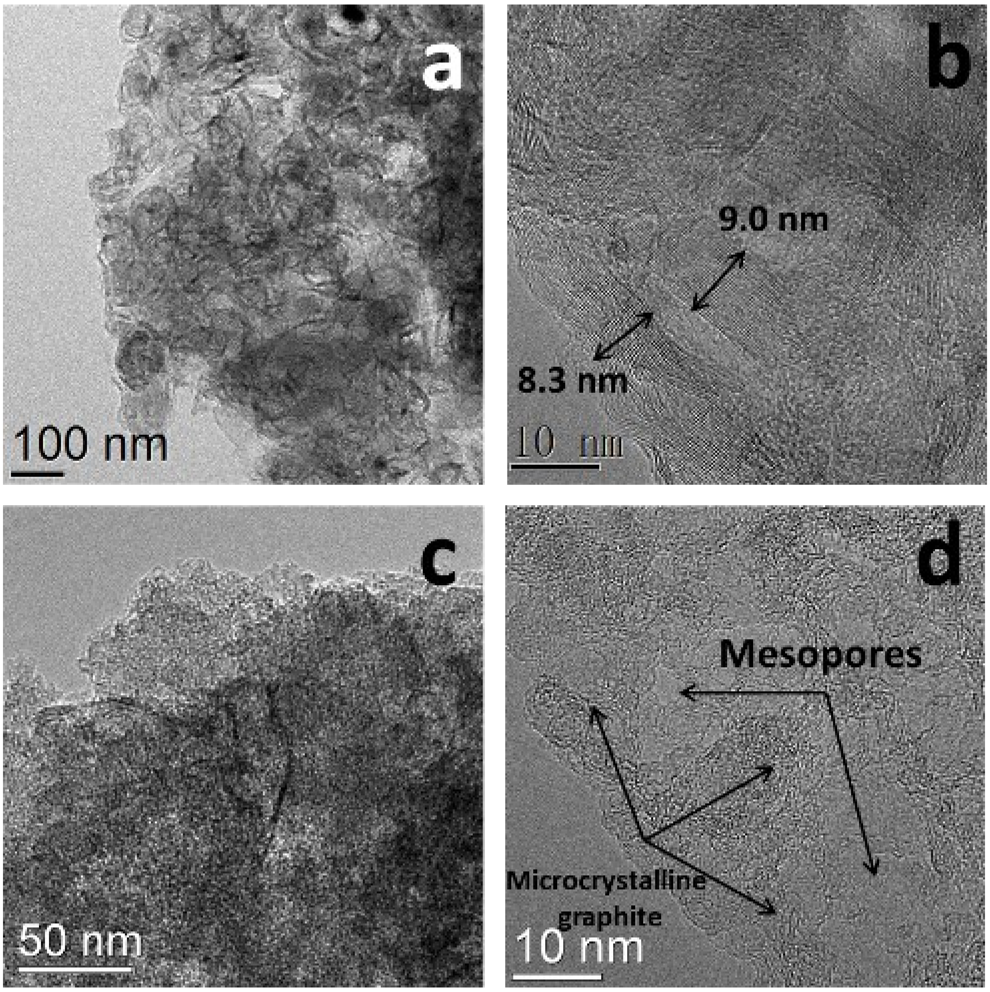

Fig. S4 TEM images of samples with different ratios of resin to KF in synthesis process. (a, b) Mass ratio of KF to resin is 0.5:1, and (c, d) mass ratio of KF to resin is 1.5:1.

Raman spectra of NFPGNS, NNG, FPGC and CC, and samples activated by KF at different temperature are shown in the Fig. S5. In the case of NFPGNS (sintered at 1000 ^{o}C), peak located at 1348 cm^{-1} corresponding to D band ascribed to the asymmetry breakdown at the edge of grapheme sheets. G band are located at 1579 cm^{-1} caused by the E_{2g} vibrational mode of the graphite layers. A 2D band at 2695 cm^{-1} based on a second-order phonon mode is presented. The Raman spectroscopies indicate high degrees graphitization of NFPGNS and NNG, which beneficial for the transport of electrons. Furthermore, intensity ratios of D band to G band and 2D band to G band are always used as tools describing the degree of grapheme structure crystalline. NFPGNS shows a very high degree of grapheme structure crystalline based on I_D/I_G of 0.502 (0.5-0.8) and I_{2D}/I_G of 0.689 (0.6-0.9) [S9] (Table S2). Meanwhile, the degrees of crystalline become higher with the temperature increased from 700 to 1000 °C. This means that the synthesis process dominated by graphitization catalyzed by Co in 700 –1000 °C. However, the crystalline degree of sample sintered at 1100 °C is a little lower than that of 1000 °C. A possible explanation is that synthesis process dominated by activation by KF after 1000 °C and more F doping level (Table S3).

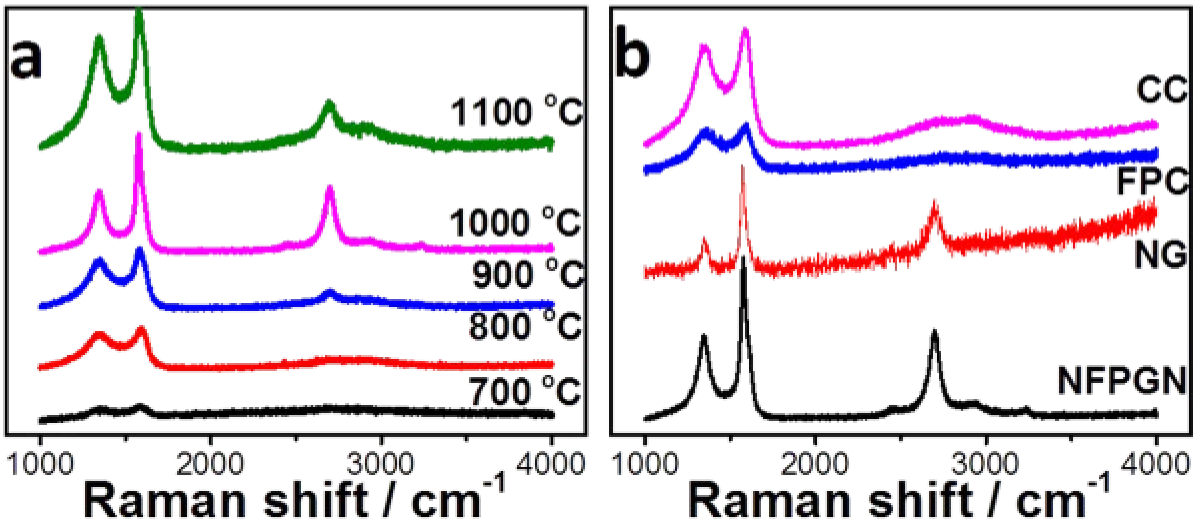

Fig. S5 Raman spectra of (a) samples of resin-$Na_3Co(NO_2)_6$-KF sintered at different temperature, and (b) NFPGNS, NNG, FPGC and CC.

Table S2 Raman shift band measurements and intensity ratios of D band to G band and 2D band to G band of NFPGNS, NNG, FPGC and CC.

	Raman shift / cm^{-1}				I_D/I_G	I_{2D}/I_G	L_a / nm
	D / cm^{-1}	G / cm^{-1}	2D / cm^{-1}	D+D’ / cm^{-1}			
NFPGNS	1348	1579	2695	2932	0.502	0.689	33.4
NNG	1348	1569	2695	N/A	0.517	0.553	32.4
FPGC	1363	1585	N/A	N/A	0.901	N/A	18.6
CC	1354	1590	N/A	N/A	0.843	N/A	19.9

Table S3 Raman shift band measurements and intensity ratios of D band to G band and 2D band to G band of samples sintered at different temperature. .

	Raman shift / cm^{-1}				I_D/I_G	I_{2D}/I_G	L_a / nm
	D / cm^{-1}	G / cm^{-1}	2D / cm^{-1}	D+D’ / cm^{-1}			
700 ^{o}C	1348	1575	N/A	N/A	0.872	N/A	19.2
800 ^{o}C	1338	1590	N/A	N/A	0.866	N/A	19.3
900 ^{o}C	1343	1585	2694	2912	0.827	0.307	20.3
1000 ^{o}C	1348	1579	2695	2932	0.502	0.689	33.4
1100 ^{o}C	1348	1579	2691	2917	0.786	0.340	21.3

The EDS pattern of NFPGNS shows the co-existence of C, N, O and F elements.

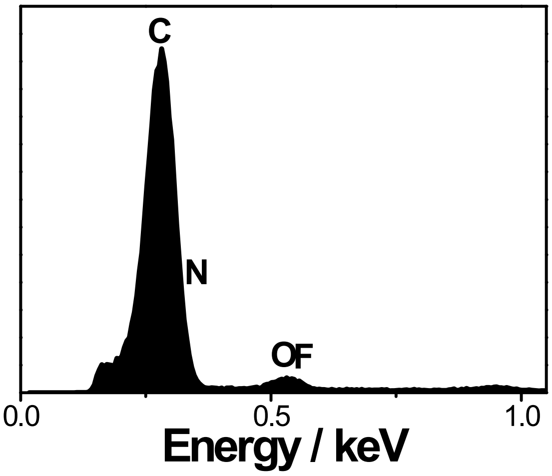

Fig. S6 The EDS pattern of NFPGNS.

XPS spectra of NFPGNS are shown in the Fig. S7. In C 1s spectrum, the peak position at 284.6 eV is corresponding to C1 attributed to sp^2 carbon, at 285.3 eV is corresponding to C2 attributed by sp^3 carbon and at 286.4 eV is attributed to C-O bond (Fig. S7a) [S10]. The peak in N 1s spectrum is attributed to three types of N: pyridinic N at 398.1 eV, pyrrolic N at 400.5 eV and graphitic N at 401.3 eV (Fig. S7b) [S11]. NFPGNS shows a pyridinic N doping rich configuration (Table S4). The peak in F 1s spectrum can be analyzed to only one structure of F: C-F bond at 687.3 eV [S12]. N-F bond has not been analyzed both in N 1s and F 1s spectrum. This means that N and F elements both doped in grapheme without interaction (Fig. S7c). In the O 1s spectrum, the peak at 534 eV corresponds to oxygen in carboxyl groups. The peak at 532 eV is for carbonyl oxygen atoms in esters, amides, carboxylic anhydrides and oxygen atoms in hydroxyls or ethers, and at 531 eV is associated with C=O groups such as ketone, lactone, and carbonyl groups (Fig. S7d) [S11].

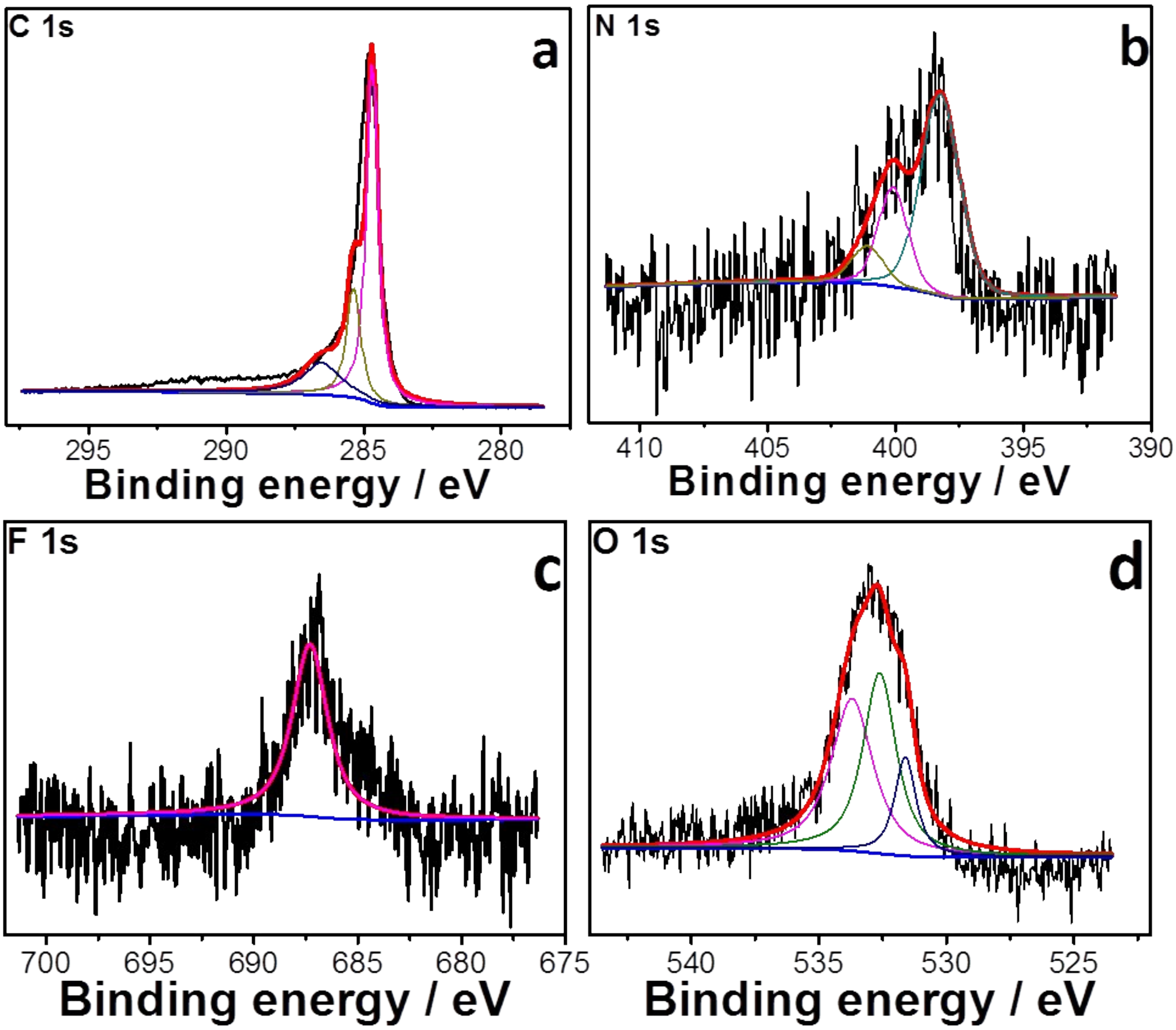

Fig. S7 XPS spectra of NFPGNS.

XPS spectra of NNG are shown in the Fig. S8. In C 1s spectrum, the peak position at 284.6 eV is corresponding to C1 attributed to sp^2 carbon, at 285.3 eV is corresponding to C2 attributed by sp^3 carbon and at 286.4 eV is attributed to C-O bond (Fig. S8a). The peak in N 1s spectrum is attributed to three types of N: pyridinic N at 398.1 eV, pyrrolic N at 400.5 eV and graphitic N at 401.3 eV (Fig. S8b). NNG shows a graphitic N doping rich configuration (Table S4). F has not been found (Fig. S8c). In the O 1s spectrum, the peak at 534 eV corresponds to oxygen in carboxyl groups. The peak at 532 eV is for carbonyl oxygen atoms in esters, amides, carboxylic anhydrides and oxygen atoms in hydroxyls or ethers, and at 531 eV is associated with C=O groups such as ketone, lactone, and carbonyl groups (Fig. S8d).

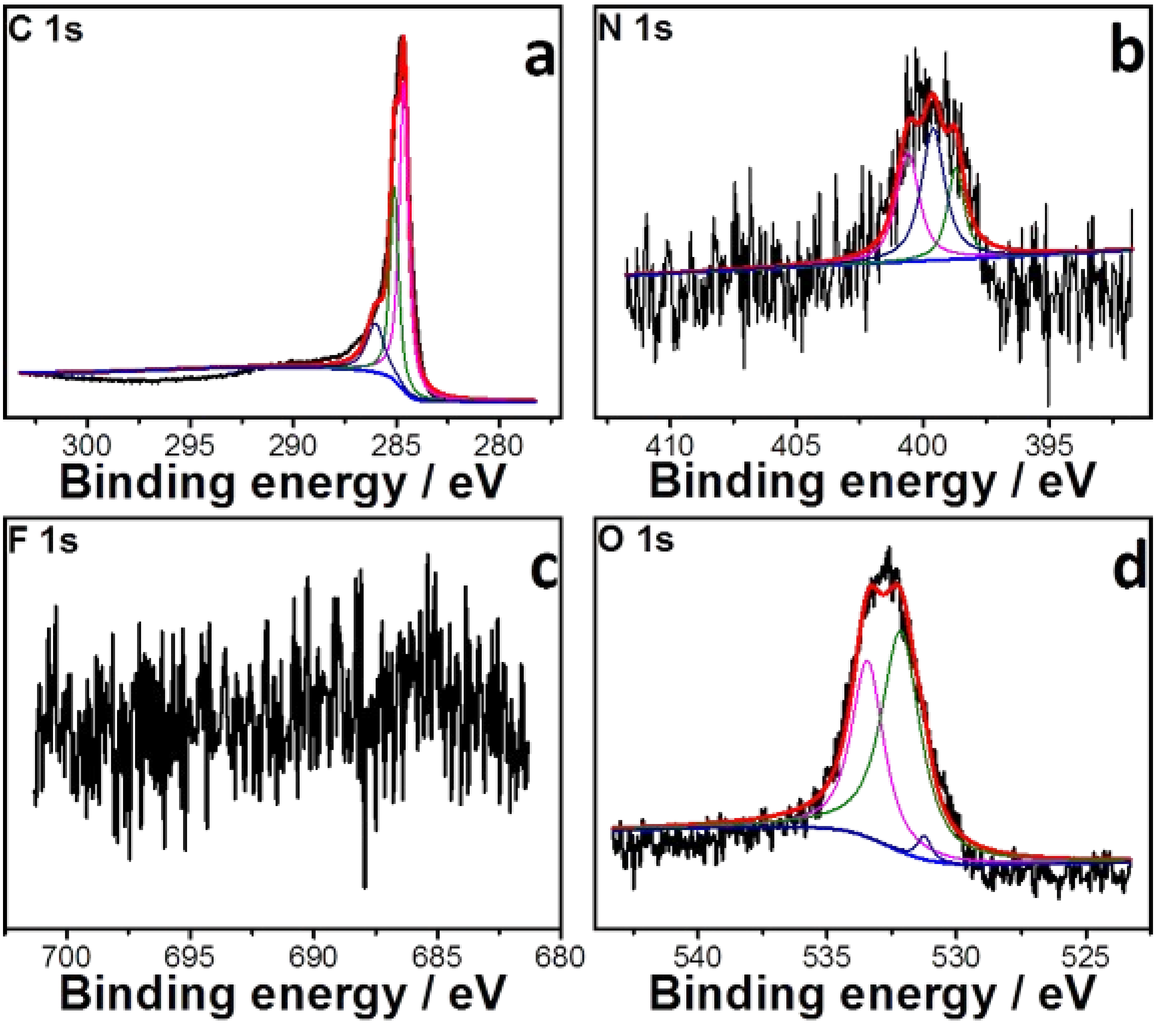

Fig. S8 XPS spectra of NNG.

XPS spectra of FPGC are shown in the Fig. S9. In C 1s spectrum, the peak position at 284.6 eV is corresponding to C1 attributed to sp^2 carbon, at 285.3 eV is corresponding to C2 attributed by sp^3 carbon and at 286.4 eV is attributed to C-O bond (Fig. S9a). N has not been found (Fig. S9b). The peak in F 1s spectrum can be analyzed to only one structure of F: C-F bond at 687.3 eV(Fig. S9c). In the O 1s spectrum, the peak at 534 eV corresponds to oxygen in carboxyl groups. The peak at 532 eV is for carbonyl oxygen atoms in esters, amides, carboxylic anhydrides and oxygen atoms in hydroxyls or ethers, and at 531 eV is associated with C=O groups such as ketone, lactone, and carbonyl groups (Fig. S9d).

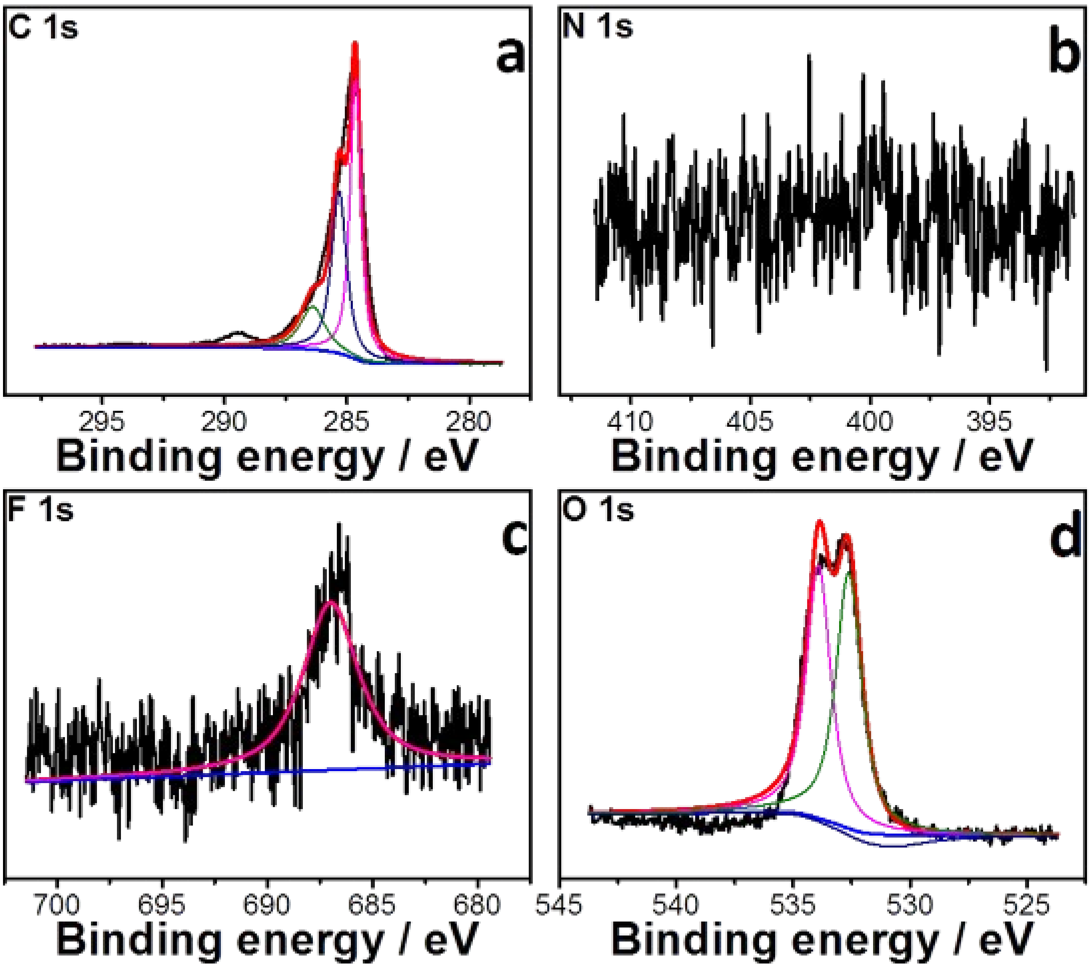

Fig. S9 XPS spectra of FPGC.

Table S4 Ratios of three types of C-N bond in NFPGNS and NNG.

	NFPGNS / %	NNG / %
Pyridinic N	64.9	24.8
Pyrrolic N	24.7	17.2
Graphitic N	10.4	58.0

NFPGNS was synthesized at 1000 ^{o}C with atomic ratio of N and F in samples of 0.89% and 0.49%, according to XPS results (Fig. S10).

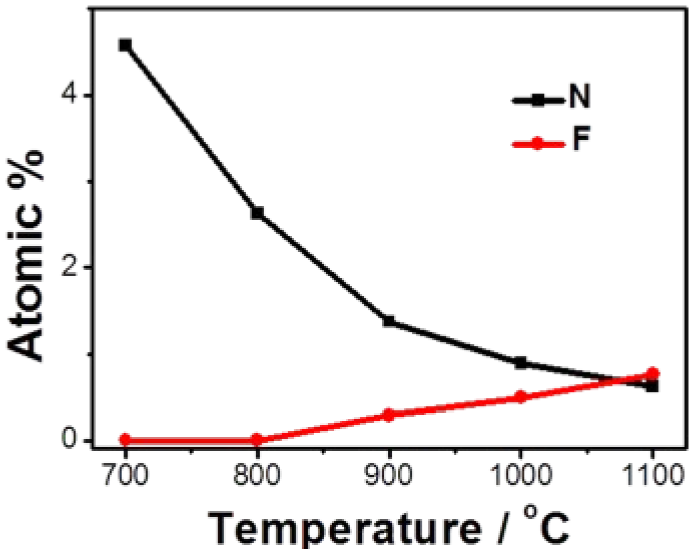

Fig. S10 Doping levels of N and F elements at different temperature.

The ratio of three N doped configurations has been found related to sintered temperature. XPS result (N 1s spectra) of samples activated by KF sintered at different temperature is shown in Fig. S11. In general, pyrrolic N generates at lower temperature (200-350 ^{o}C), transforming to pyridinic N at 550-750 ^{o}C and finally converting to graphitic N above 750 ^{o}C^{S13}. In this work, Pyridinic N (py-N) and Pyrrolic N (pr-N) were observed as dominated N doping configurations at lower temperature of 700 and 800 ^{o}C (Fig. S11). The content of graphitic N configuration increased with graphitization degree becoming higher at 900 ^{o}C, indicating pyridinic N transforming to graphtic N configuration. However, content of graphitic N decreased under chemical-etching by KF at higher temperature (1000 and 1100 ^{o}C), transforming to pyridinic N. Meanwhile, unstable pyrrolic N doping configurations converts to other doping configurations$^{S13, S14}$. Therefore, pyrrolic and pyridinic N dominated doping configurations can be synthesized at lower temperatures and pyridinic N doping rich configurations can be obtained at higher temperatures. However, graphitic N dominated doping configurations are difficult to obtain at the situation activated by KF.

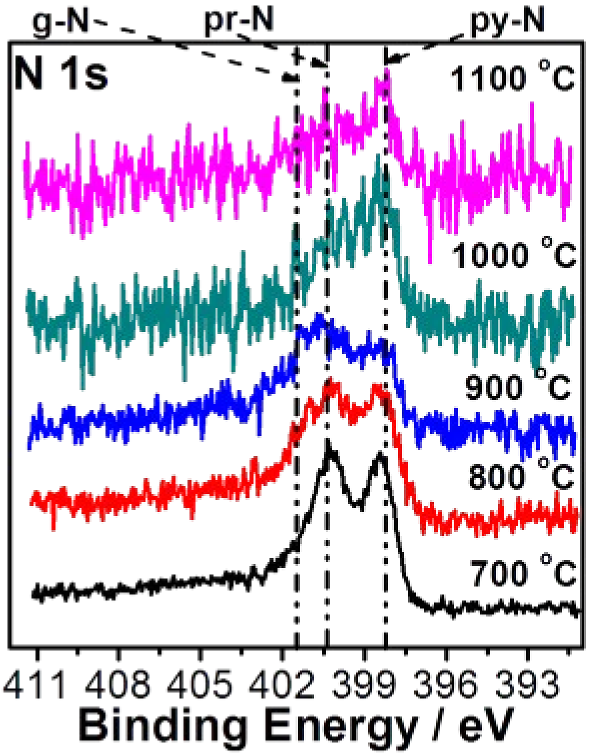

Fig. S11 XPS spectra of samples sintered at different temperature.

Fig. S12a shows the CV curves of NFPGNS in 1 M KOH with different scan rate. There is no remarkable peak in these curves and the highest specific capacity is 358 mF/cm^{-2} at 1 mV/s. The linear relationship between specific capacities and square roots of scan rate indicates that charge/discharge of supercapacitors controlled by a diffusion-limited process [S15].

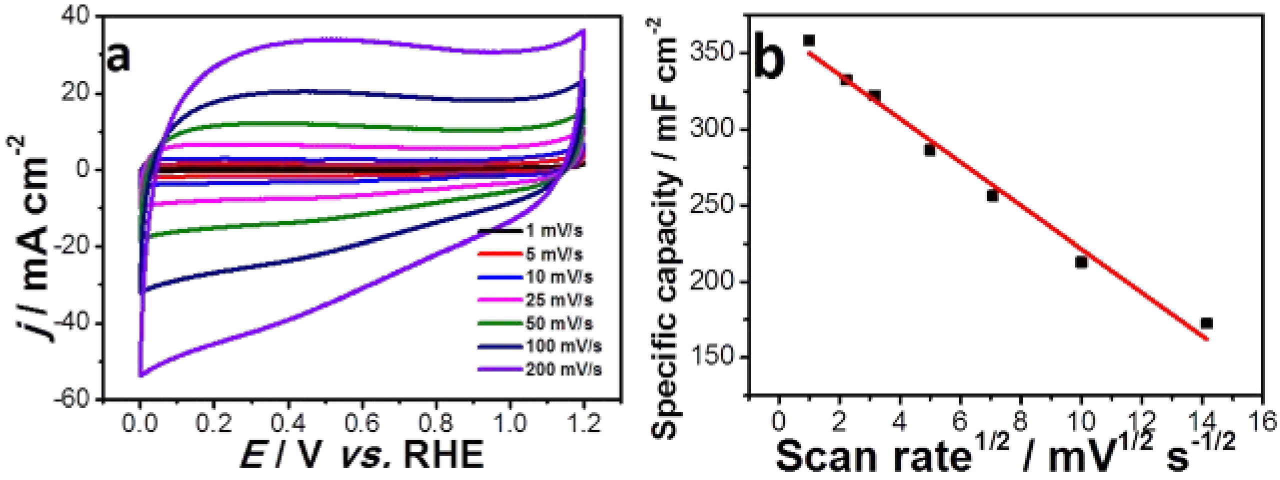

Fig. S12 (a) CV curves of NFPGNS in 1 M KOH at 25 °C with different scan rate. (b) Relationship between specific capacities and square roots of scan rate.

A three-electrode-system was used for electrochemical measurements of HER and OER on NFPGNS, NNG, FPGC, CC and Pt/C electrocatalysts (Fig. S13a). The multi-step chronoamperometric curve for HER on NFPGNS electrocatalysts started at 50 mV *vs.* RHE and ended at -400 mV *vs.* RhE, with a decrement of 25 mV per step for 3 min from 50 mV to 0 mV and a decrement of 10 mV per step for 3 min from 0 mV to -400 mV without *iR*-correction (Fig. S13b). In the case of OER on NFPGNS electrocatalysts, the multi-step chronoamperometric curve started at 1.35 V *vs.* RHE and ended at 1.63 V *vs.* RhE, with a decrement of 10 mV per step for 3 min without *iR*-correction (Fig. S13c). A two-electrode-system was used for electrochemical measurement of overall water splitting on NFPGNS, NNG, FPGC, CC and Pt/C electrocatalysts (Fig. S13d). The multi-step chronoamperometric curve of overall water splitting on NFPGNS electrocatalysts started at 1.45 V and ended at 2 V with a decrement of 10 mV per step for 3 min without *iR*-correction was shown in Fig. S13e.

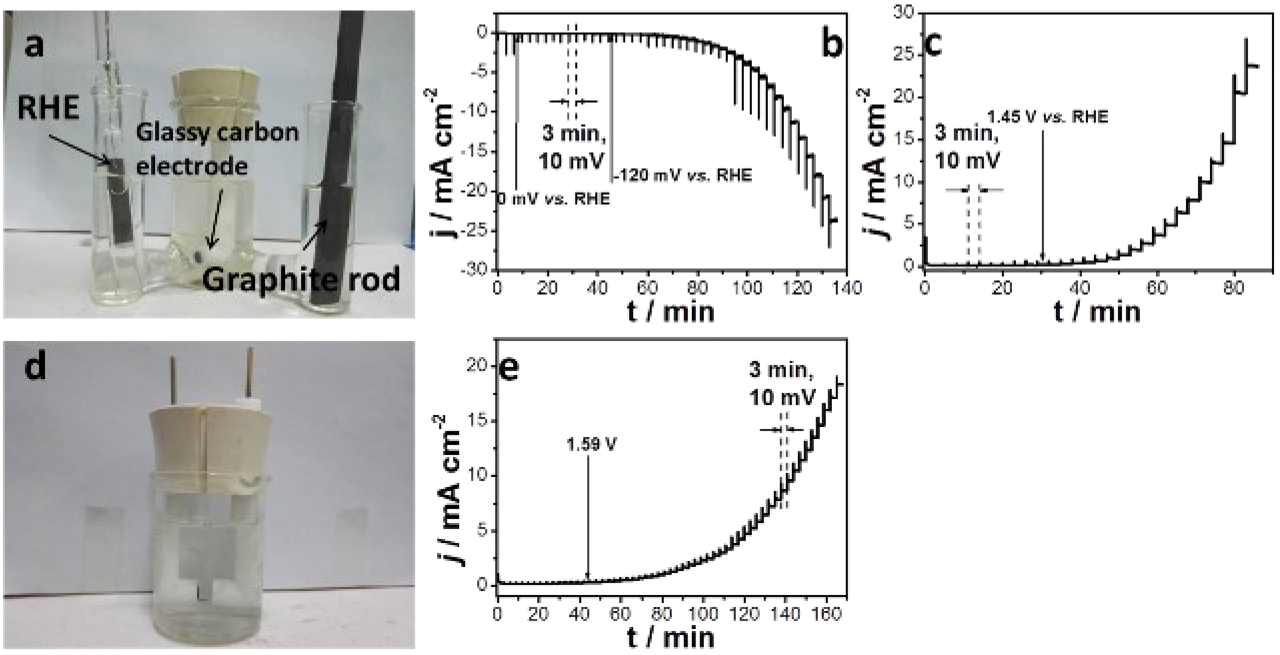

Fig. S13 (a) A three-electrode-system was used for electrochemical measurements of HER and OER. (b) and (c) The multi-step chronoamperometric curves for HER and OER of NFPGNS electrocatalysts. (d) A two-electrode-system was used for electrochemical measurement of overall water splitting. (e) The multi-step chronoamperometric curve for overall water splitting reaction on NFPGNS electrocatalysts.

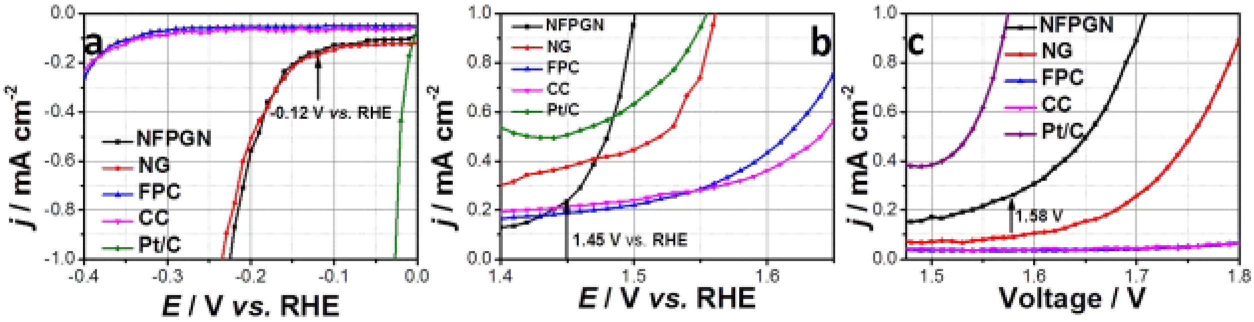

Fig. S14 Steady-state polarization curves foe (a) HER, (b) OER and (c) water splitting on NFPGNS, NNG, FPGC, CC and Pt/C electrocatalysts at current density ranges up to (-)1 mA cm^{-2}.

Table S5 HER performance on metal free electrocatalysts.

Catalyst	Electrolyte	Onset potential / V	Tafel slope / mV/dec	*j_0* / mA/cm^{-2}	*η* @ 10 mA cm^{-2} / V	Reference
N, P doped Graphene	0.5 M H_2SO_4	-0.29	91	2.4×10^{-4}	-0.42	ACS Nano, 2014, 8, 5290 .
N, S co-doped Graphene	0.5 M H_2SO_4	-0.22	105	N/A	-0.385	Angew. Chem. Int. Ed., 2015, 54, 2131.
B-SuG	0.5 M H_2SO_4	~ -0.20	99	1.4×10^{-3}	N/A	Catal. Sci. Technol., 2014, 4, 2023.
C_3N_4@NG	0.5 M H_2SO_4	N/A	51.5	3.5×10^{-4}	~ -0.240	Nat. Commun.; 2014, 5, doi:10.1038/ncomms4783.
ONPPGC/	1 M KOH	N/A	154	N/A	-0.446	Energy

OCC						Environ. Sci., 2016, 9, 1210.
$C_{60}(OH)_8$	0.5 M H_2SO_4	-0.16	103	N/A	N/A	Angew. Chem. Int. Ed. 2013, 52, 10867.
N doped Activated Carbon	1 M NaOH	N/A	N/A	N/A	-0.625	RSC Adv., 2014, 4, 4916
Activated carbon nanotubes	0.5 M H_2SO_4	-0.10	71.3	1.6×10^{-2}	N/A	Chem. Commun., 2014, 50, 9340.
NFPGNS	1 M KOH	-0.12	109	1.847×10^{-2}	-0.33	This work
NNG	1 M KOH	-0.12	134	8.735×10^{-3}	-0.37	This work
FPGC	1 M KOH	~ -0.30	212	2.413×10^{-3}	N/A	This work
CC	1 M KOH	~ -0.30	191	1.743×10^{-3}	N/A	This work
Pt/C	1 M KOH	~0	30	1.869×10^{-1}	-0.10	This work

The catalytic activities on samples activated by KF sintered from 700 to 1100 ^{o}C toward HER and OER have been performed (Fig. S15). Sample sintered at 900, 1000 and 1100 ^{o}C show best HER onset potentials of ~ 0.12 V, better than that of sintered at lower temperatures. This may be based on the higher degree of graphitization presented at higher temperatures. Meanwhile, samples with appropriate amount of doping N and F and pyridinic N dominated doping configurations showed best catalytic activities (Fig. S10 and 11). The amount of doping F increased and N decreased sintered at 1100 °C than that of 1000 °C. However, sample sintered at 1100 °C performed worse on HER than that of 1000 °C. This indicates that higher amount of F doped in carbon materials is detrimental to improve the HER performance, and this is also proved on FPGC electrocatalysts. This effect has been also observed for OER.

NFPGNS sintered at 1000 °C exhibited best catalytic performance based on pyridinic N becoming dominated doping configuration at 1000 and 1100 °C, which has been considered as most active doping configuration (Fig. S11). Samples sintered below 900 °C exhibit worse catalytic activities; although pyridinic N and pyrrolic N dominated doping configurations and higher N doping level was observed. This is because that F has not doped in graphene or doping level is too little. The purpose of F doping in this work is increasing catalytic activities of N doped graphene by introducing modified electron acceptor-donor properties of carbons by synergistically coupling effect between heteroatoms with large number of C sites serving as active sites to adsorb adsorbates. However, it has been reported that fluorine modifies electronic properties of graphene by reducing the charge in conducting π orbitals with band gap level increased[S16]. This is detrimental to conductivity and even catalytic performance of F doped graphene. In fact, F doped sample and NFPGNS sintered at 1100 °C with F as dominated heteroatoms showed worst performance.

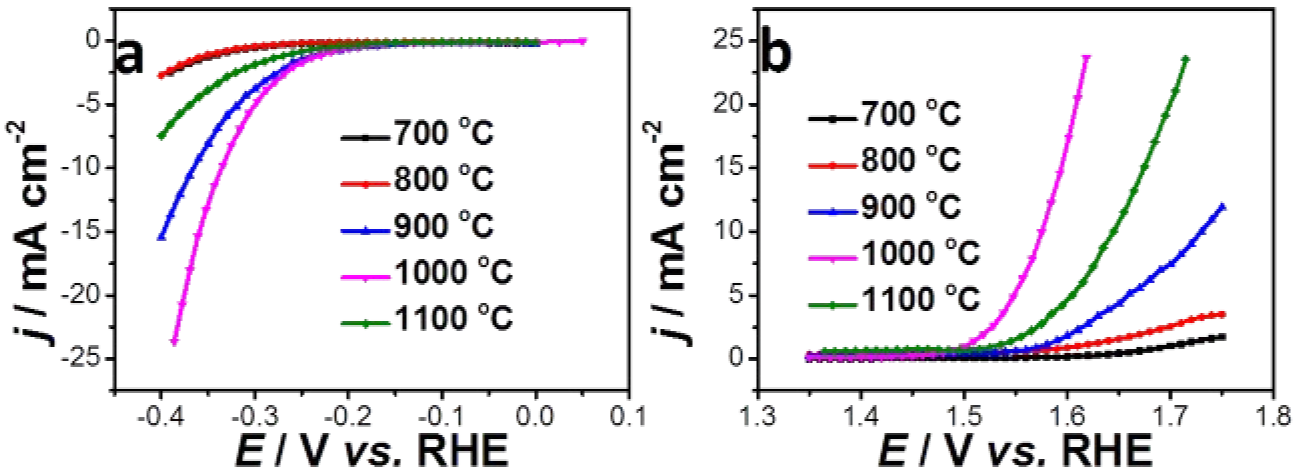

Fig. S15 Steady-state polarization curves of sanples activated by KF sintered at different temperatures for (a) HER and (b) OER.

Table S6 OER performance on metal free electrocatalysts.

Catalyst	Electrolyte	Onset potential / V	Tafel slope / mV/dec	j_0 / mA/cm^{-2}	η @ 10 mA cm^{-2} / V	Reference
NGSH	1 M KOH	N/A	83	N/A	1.63	Small 2014, 10, 2251
N-GRW	C	N/A	47	N/A	1.59	Science Advances, 2016, 2, e1501122
ONPPGC/OCC	1 M KOH	N/A	83	N/A	1.64	Energy Environ.

						Sci., 2016, 9, 1210
CNNT-ACN	0.1 M KOH	N/A	330	N/A	1.68	ACS Appl. Mater. Interfaces 2015, 7, 11991.
N-PC@G-0.02	0.1 M KOH	N/A	78	N/A	1.63	Carbon, 2016, 106, 74e83
NFPGNS	1 M KOH	1.45	78	1.666×10^{-2}	1.57	This work
NNG	1 M KOH	1.53	109	9.586×10^{-4}	1.72	This work
FPGC	1 M KOH	> 1.60	159	1.709×10^{-3}	N/A	This work
CC	1 M KOH	> 1.60	230	4.005×10^{-4}	N/A	This work
Pt/C	1 M KOH	1.52	99	4.642×10^{-4}	1.67	This work

Table S7 Overall water splitting activities of NFPGNS, NNG, FPGC, CC and Pt/C electrocatalysts.

	Voltage for overall water splitting / V	Voltage for overall water splitting @ 10 mA cm^{-2}/ V
NFPGNS	1.58	1.91
NNG	1.65	N/A

FPGC	N/A	N/A
CC	N/A	N/A
Pt/C	1.52	1.77

In the two-time constant model (Fig. S16), R_s is the series resistance, R_{ct} denotes the charge transfer resistance, R_p related to is the porosity the electrode surface, and the double layer capacitance is represented by the elements CPE_1 and CPE_2. [S17-S19]

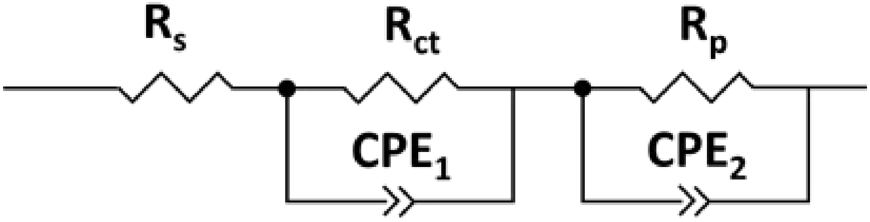

Fig. S16 A two-time constant model for fitting the EIS response of HER and OER on NFPGNS, NNG, FPGC and CC electrocatalysts.

The resulting Nyquist plots of the NFPGNS, NNG, FPGC and CC electrocatalysts were performed to explore the HER electrode kinetics.[S20] Experimental data were fitted using a two-time constant model shown in Fig. S16[S21, S22] (Fig. S17a-d). In Fig. S17e, the charge-transfer resistance, R_{ct}, is found to be overpotential-dependent. NFPGNS and NNG electrocatalysts exhibited much lower charge transfer impedances (2.1 and 9.9 Ω) than that of FPGC and CC (600.2 and 141.2 Ω) at -0.4 V *vs.* RHE. This result suggests that NFPGNS and NNG afford faster electron transport from the active site, than samples without N doping.

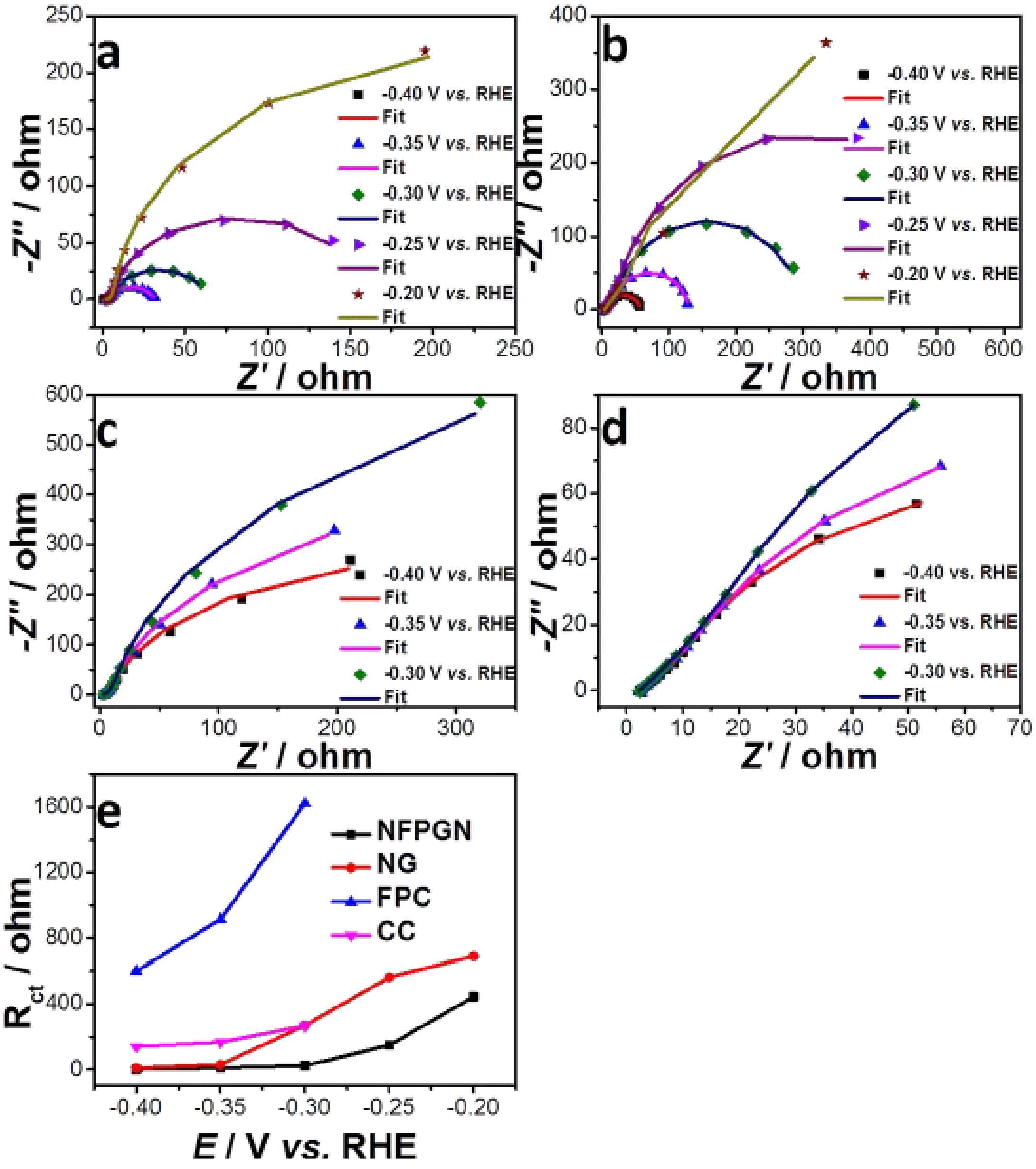

Fig. S17 The Nyquist plots and fittings for the impedance response of (a) NFPGNS, (b) NNG, (c) FPGC and (d) CC electrocatalysts toward HER. (e) Dependence of the charge-transfer resistance (R_{ct}) on the overpotential of NFPGNS, NNG, FPGC and CC electrocatalysts.

The resulting Nyquist plots of the NFPGNS, NNG, FPGC and CC electrocatalysts were performed to explore the OER electrode kinetics [S19]. Experimental data were fitted using a two-time constant model shown in Fig. S16 (Fig. S18a-d). In Fig. S18e, the charge-transfer resistance, R_{ct}, is found to be overpotential-dependent. NFPGNS and NNG electrocatalysts exhibited much lower charge transfer impedances (9.7 and 19.7 Ω) than that of FPGC and CC (110.7 and 132.4 Ω) at 1.75 V *vs.* RHE. This result suggests that NFPGNS and NNG afford faster electron transport from the active site, than samples without N doping.

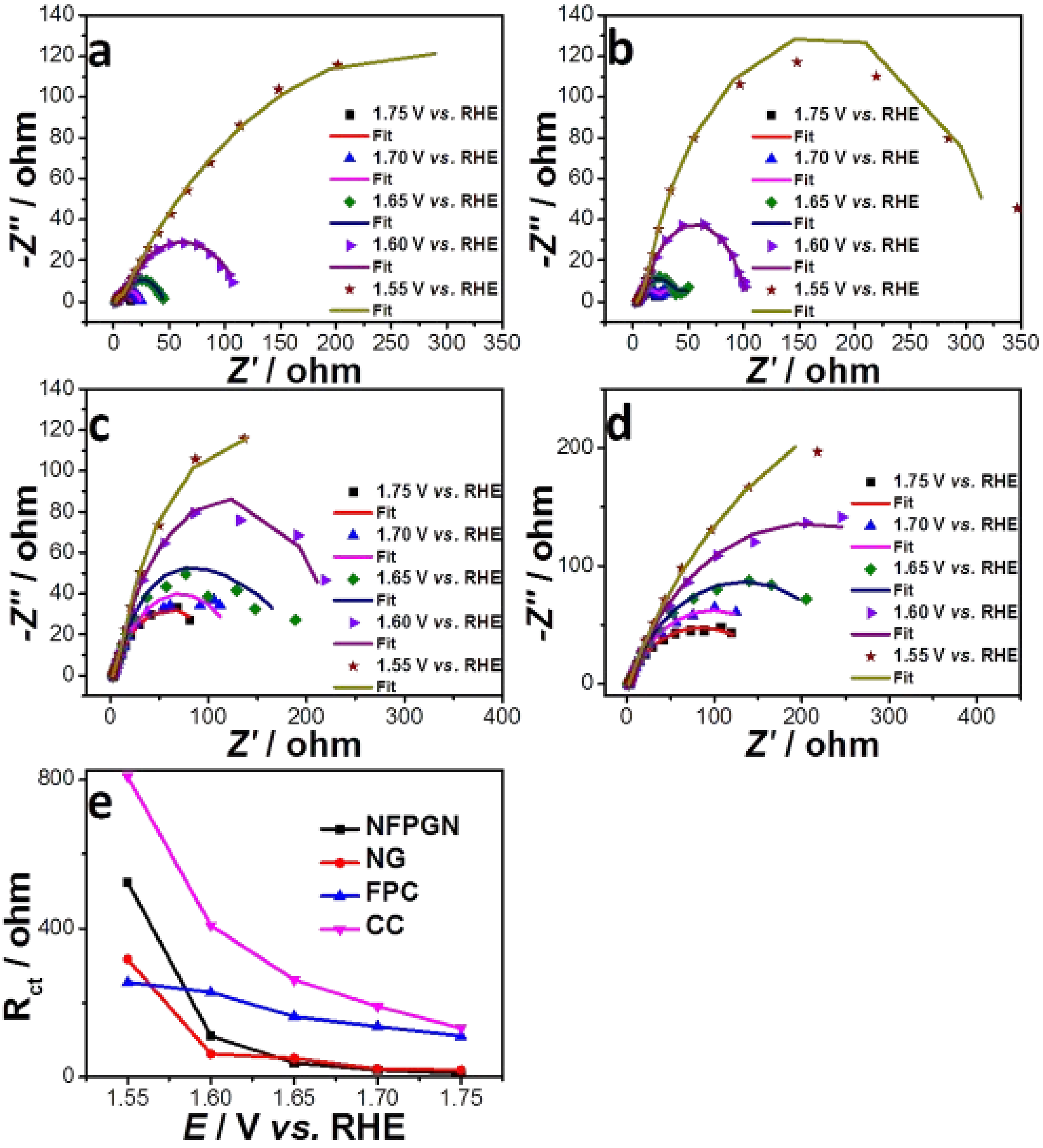

Fig. S18 The Nyquist plots and fittings for the impedance response of (a) NFPGNS, (b) NNG, (c)

FPGC and (d) CC electrocatalysts toward OER. (e) Dependence of the charge-transfer resistance (R_{ct}) on the overpotential of NFPGNS, NNG, FPGC and CC electrocatalysts.

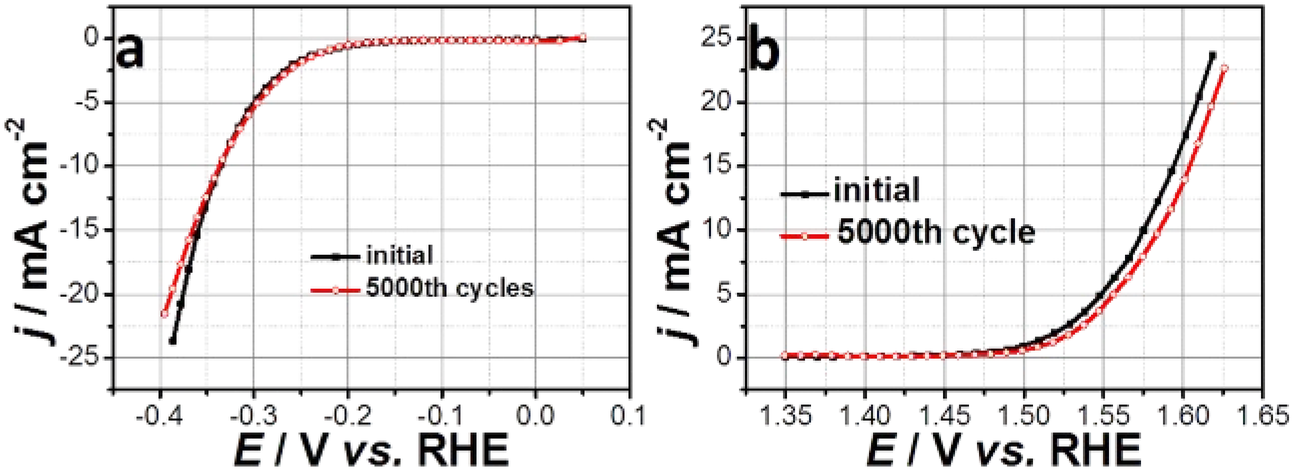

Fig. S19 Steady-stated polarization curves of NFPGNS electrocatalysts for (a) HER and (b) OER initially and after 5000 cycles in 1 M KOH at 25 °C.

Results of stabilities test at higher potentials and voltage are shown in Fig. S20. Chronoamperometric profiles of HER and OER on NFPGNS electrocatalysts at -0.37 and 1.60 V *vs.* RHE are shown in Fig. S20a. Initial current densities of NFPGNS electrocatalysts for HER and OER are -20.0 and 20.0 mA cm^{-2}, decreased to -17.6 and 16.2 mA cm^{-2} after 18 h. The chronoamperometric profile of NFPGNS electrocatalysts for water splitting at 2.01 V is shown in the Fig. S20b with an initial current density of 20.0 mA cm^{-2}, and gradually decreased to 16.6 mA cm^{-2} after 12 h.

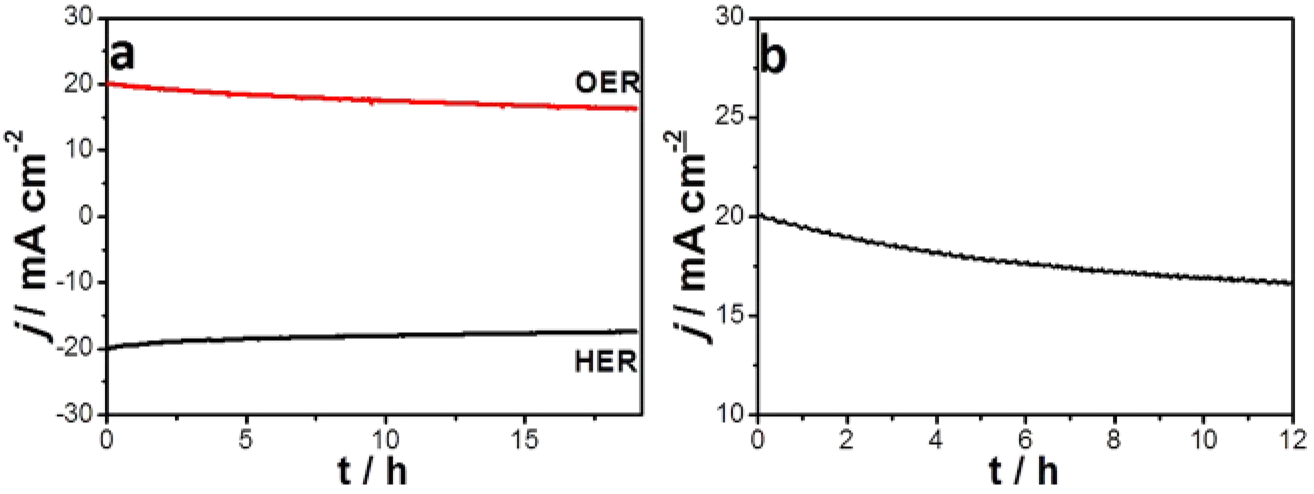

Fig. S20 Chronoamperometric plots of HER at -0.37 V *vs.* RHE, OER at 1.60 V *vs.* RHE and water splitting at 2.0 V on NFPGNS electrocatalysts in 1 M KOH at 25 °C.

The morphology, structure and composition of NFPGNS as electrocatalysts for OER after stability test were studied by SEM, XPS and XRD analyses (Fig. S21-23). After stability test, NFPGNS still exhibited typical sheet like morphology. NFPGNS was proved as N and F dual doped structure after stability test according to that XPS peak position was almost identical to the sample before used as catalysts for OER. The graphite (002) peak was observed on NFPGNS used as catalysts before and as electrocatalysts for OER after stability test, and there is no other peaks appeared in XRD pattern of sample after stability test. It means that the morphology, structure and composition of NFPGNS are not changed after used as electrocatalysts for OER, indicating superior structural stability.

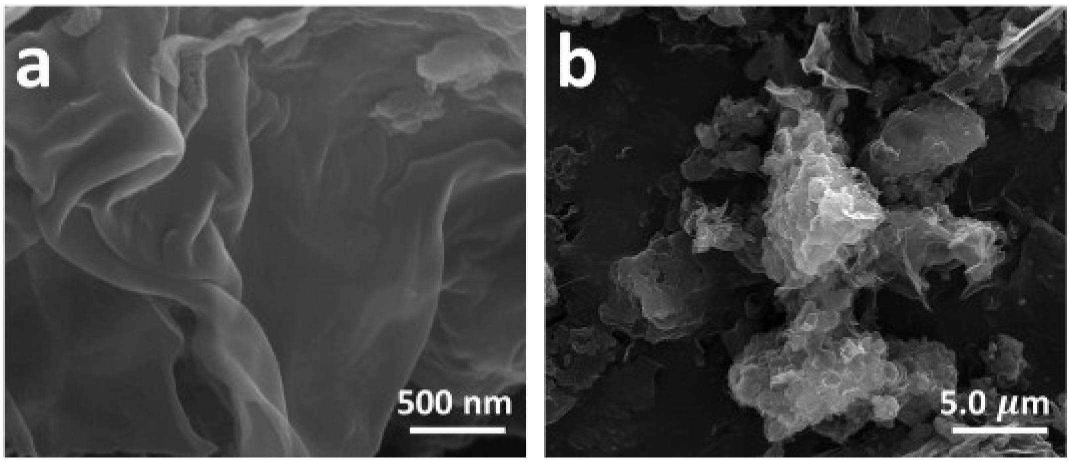

Fig. S21 SEM images of NFPGNS before and after used as catalysts for OER.

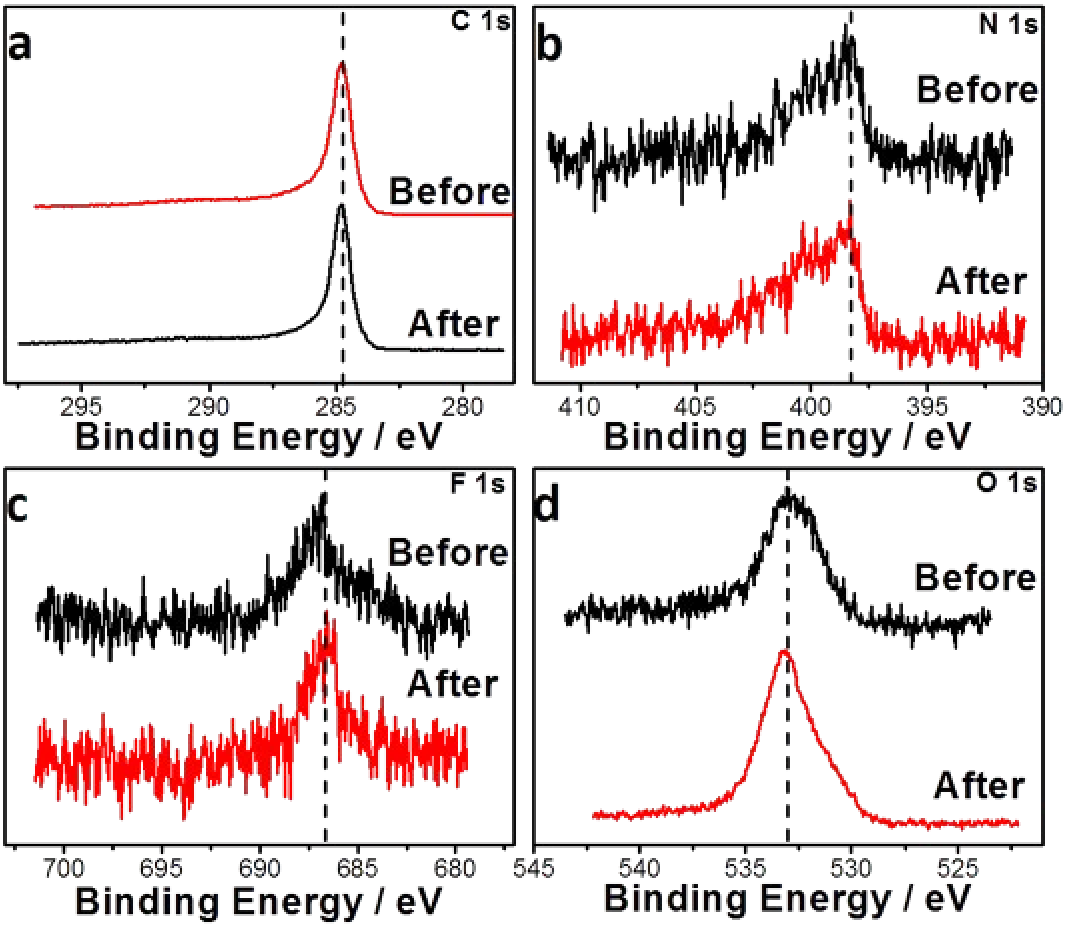

Fig. S22 XPS spectra of NFPGNS before and after used as catalysts for OER.

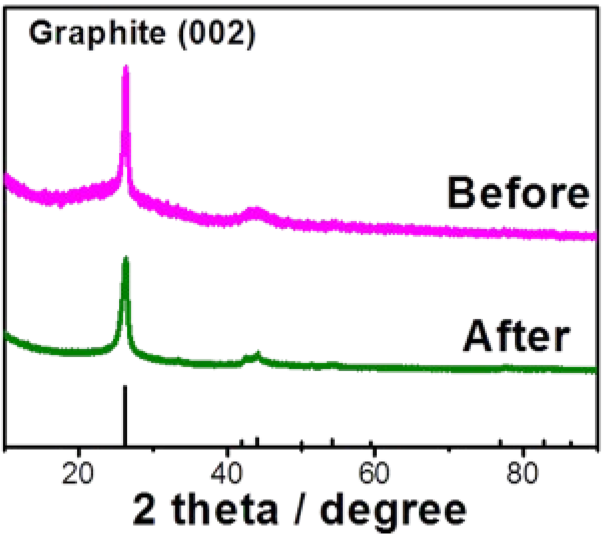

Fig. S23 XRD patterns of NFPGNS before and after used as catalysts for OER.

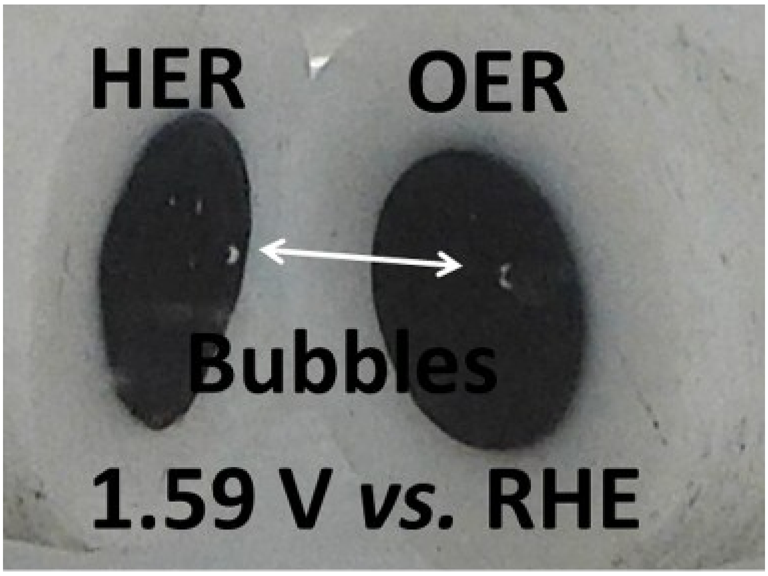

Fig. S24 The image of water splitting on NFPGNS electrocatalysts at 1.59 V with bubbles of O_2 and H_2 appeared.

Heteroatoms doped carbon materials have been widely researched and applied in electrocatalytic filed after Dai *et al.* first report N doped CNT as efficient metal free electrocatalysts for ORR[S23].

Heteroatoms obviously tuned the electronic structure of graphene, including Fermi level, spin density, band gap, work function and so on. Doping N has been considered as electron acceptor based on higher electronegativity than C. Thus, it has been considered that positive charge distributed around C sites neighbored N sites, beneficial for adsorption of adsorbents[S24]. However, it has been reported that fluorine modifies electronic properties of graphene by reducing the charge in conducting π orbitals with band gap level increased [S16]. This is detrimental to conductivity and even catalytic performance of graphene. In fact, F doped sample shows slight catalytic activities towards HER and OER in this work, indicating that F could not be as dominated heteroatoms in doped graphene with higher catalytic activities. Various heteroatoms (including N) co- and tri-doped carbon materials exhibit good catalytic activities towards HER, OER and ORR [S25-27]. The purpose of F doping in this work is increasing catalytic of N doped graphene by introducing modified electron acceptor-donor properties of carbons by synergistically coupling effect between heteroatoms with large number of C sites serving as active sites to adsorb adsorbents.

Mulliken charge distributions of C sites after heteroatoms doped in graphene based on introducing modified electron acceptor-donor properties of carbons by synergistically coupling effect between heteroatoms [S28, S29]. In general, origin of OER on carbon based materials have been considered from higher charge density distributed on carbon around heteroatoms, in favor of adsorption for OH*, O* and OOH*, by introducing electronegative N and F atoms. [S28, S30] After heteroatoms doped, negative charge transfer to N and F atoms based on most electronegative and positive charge transfer to C sites around heteroatoms. Most positive transport to C are shown in N and F dual doped graphene (0.410 e for pyN, F-G and 0.478 e for gN, F-G) (Fig. S25a and c). Meanwhile, positive charge transport to C is also observed in N doped graphene (0.167 e for pyN-G and 0.211 e for gN-G) and F doped graphene (0.364 e). However, the most positive charge distribution on C of G is 0.023 e.

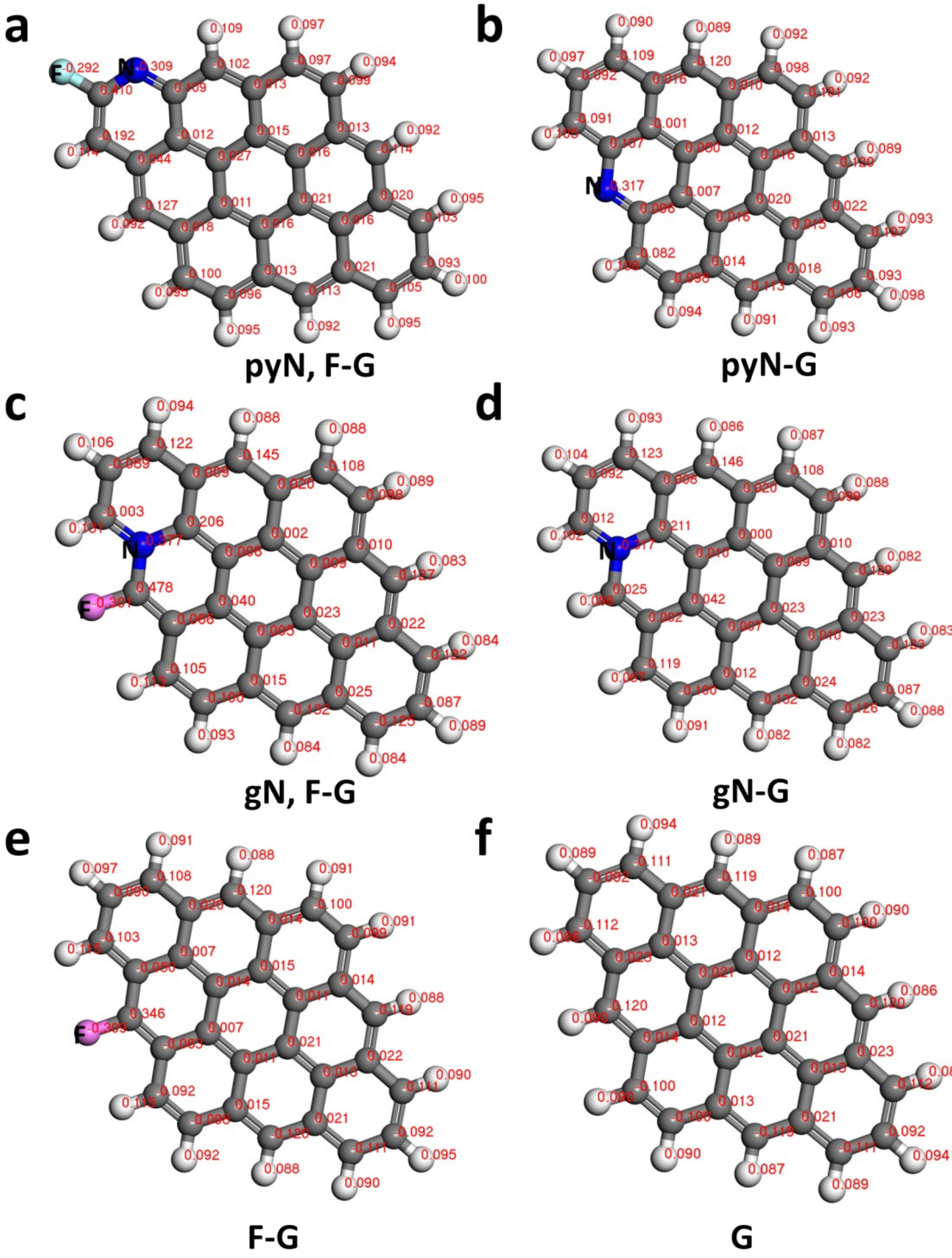

pyN, F-G

pyN-G

gN, F-G

gN-G

F-G

G

Fig. S25 Atomic structures Mulliken charge distributions of (a) pyN, F-G, (b) pyN-G, (c) gN, F-G, (d) gN-G, (e) F-G and (f) G.

E_p of N and F dual doped graphene (-6.87 eV for pyN, F-G and -7.75 eV for gN, F-G) is obviously highest than others on DOSs of active carbon adsorbed with H*. Meanwhile, E_p of N doped graphene (-8.09 eV for pyN-G and -8.14 gN-G) is higher than that of F doped graphene (-8.52 eV) and graphene (-8.70 eV). Moreover, pyridinc N doped graphene models show higher E_p than that of graphitic N doped models, indicating stronger adsorption strength and consequently lower value of $|\Delta G|$. In other words, pyridinc N doped and pyridinc N and F dual doped graphene show better performance towards HER (Fig. S26).

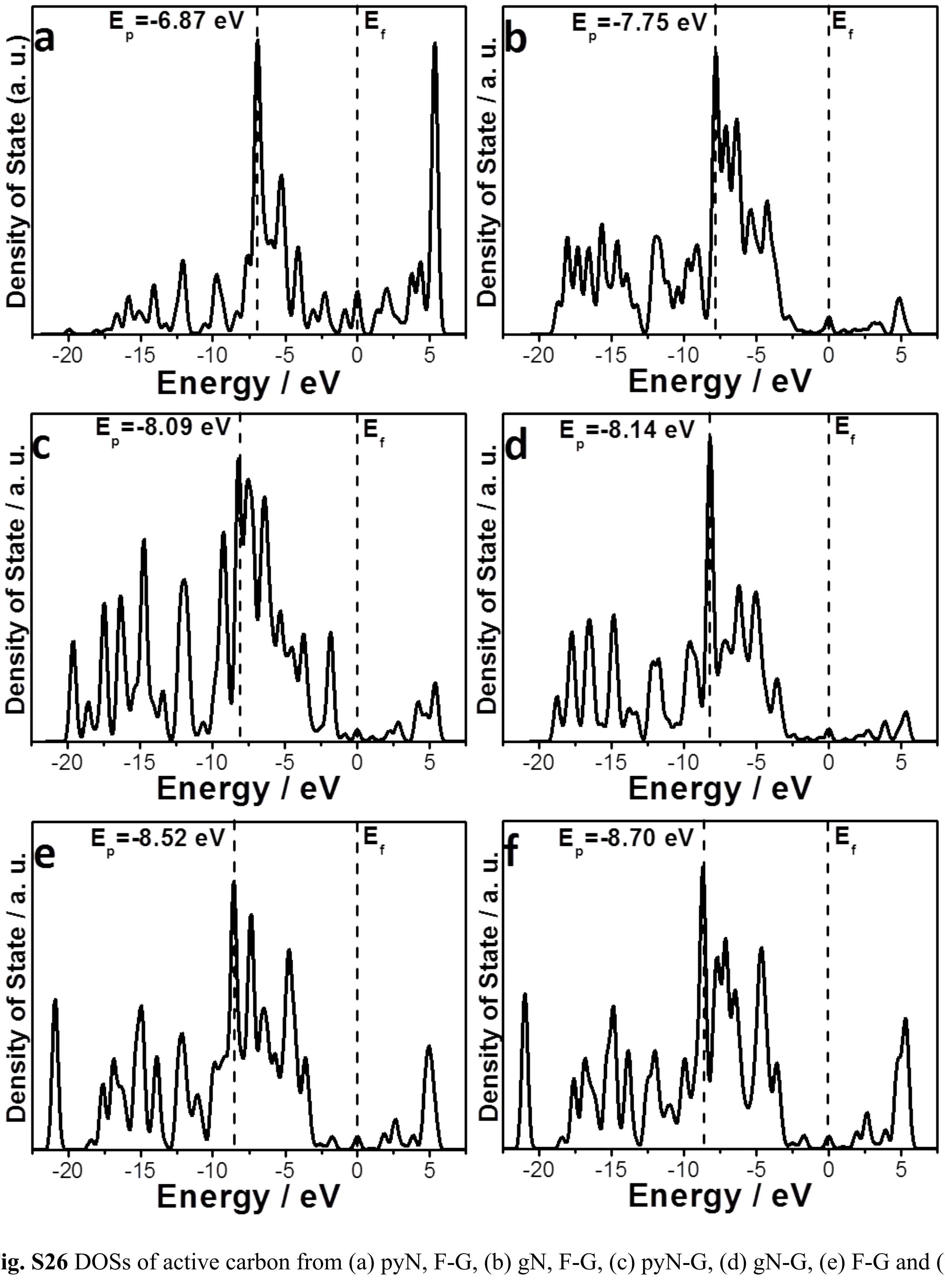

Fig. S26 DOSs of active carbon from (a) pyN, F-G, (b) gN, F-G, (c) pyN-G, (d) gN-G, (e) F-G and (f) G with H adsorption.

E_p of N and F dual doped graphene (-5.97 eV for pyN, F-G and -7.26 eV for gN, F-G) is obviously highest than others on DOSs of active carbon adsorbed with OH*. Meanwhile, E_p of N doped graphene (-8.20 eV for pyN-G and -8.70 gN-G) is higher than that of F doped graphene (-8.75 eV) and graphene (-9.24 eV). Moreover, pyridinc N doped graphene models show higher E_p than that of graphitic N doped models, indicating stronger adsorption strength and consequently lower value of $|\Delta G|$ (Fig. S27).

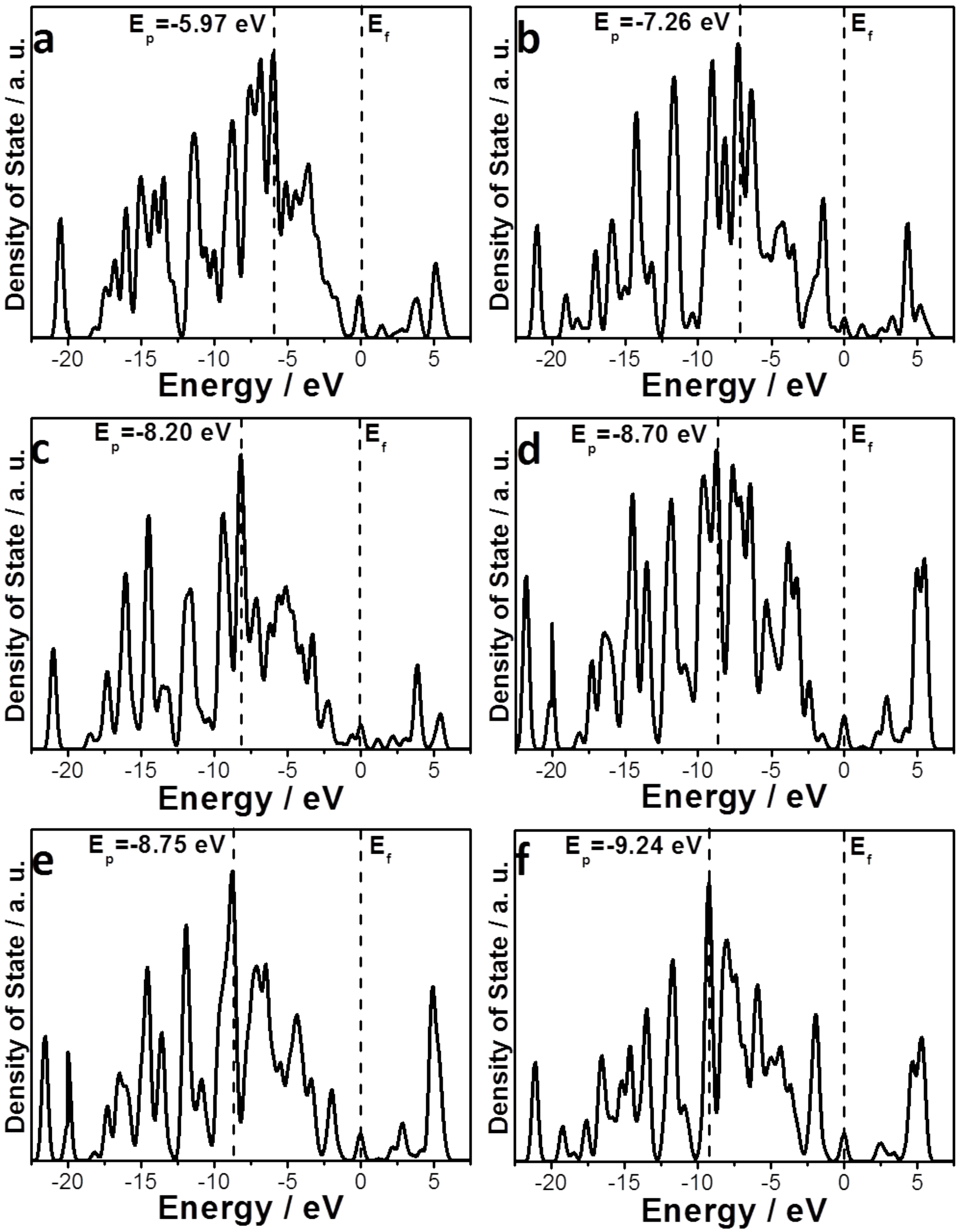

Fig. S27 DOSs of active carbon from (a) pyN, F-G, (b) gN, F-G, (c) pyN-G, (d) gN-G, (e) F-G and (f) G with OH adsorption.

E_p of N and F dual doped graphene (-4.64 eV for pyN, F-G and -5.14 eV for gN, F-G) is obviously highest than others on DOSs of active carbon adsorbed with O*. Meanwhile, E_p of N doped graphene (-7.16 eV for pyN-G and -9.04 gN-G) is higher than that of F doped graphene (-9.44 eV) and graphene (-11.23 eV). Moreover, pyridinc N doped graphene models show higher E_p than that of graphitic N doped models, indicating stronger adsorption strength and consequently lower value of $|\Delta G|$ (Fig. S28).

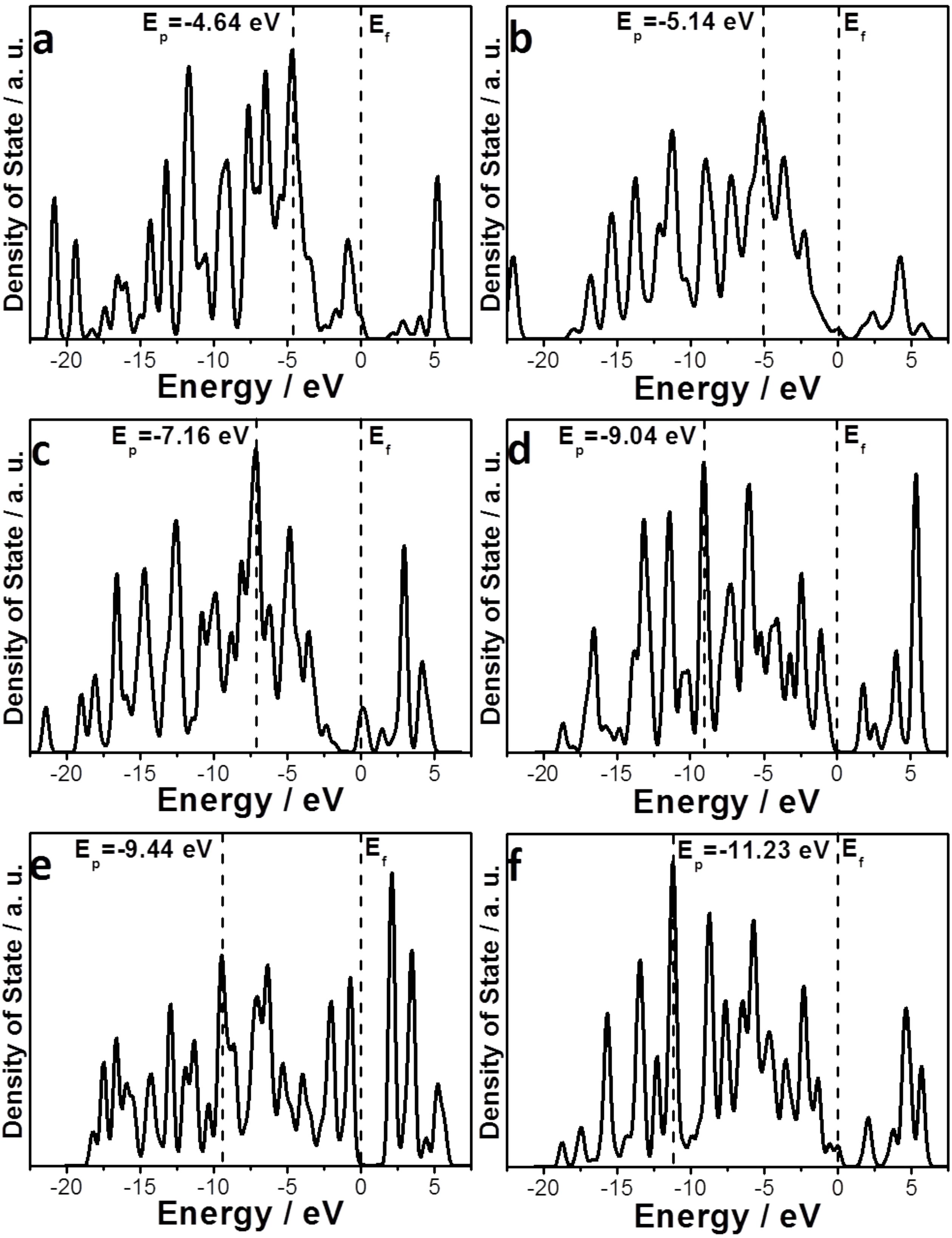

Fig. S28 DOSs of active carbon from (a) pyN, F-G, (b) gN, F-G, (c) pyN-G, (d) gN-G, (e) F-G and (f) G with O adsorption.

E_p of N and F dual doped graphene (-3.89 eV for pyN, F-G and -5.43 eV for gN, F-G) is obviously highest than others on DOSs of active carbon adsorbed with OOH*. Meanwhile, E_p of N doped graphene (-5.97 eV for pyN-G and -6.07 gN-G) is higher than that of F doped graphene (-9.14 eV) and graphene (-11.92 eV). Moreover, pyridinc N doped graphene models show higher E_p than that of graphitic N doped models, indicating stronger adsorption strength between carbon active sites and OH*, O* and OOH* leading to consequently lower values of $|\Delta G|$ for OH*, O* and OOH*. In other words, pyridinc N doped and pyridinc N and F dual doped graphene show better performance towards OER (Fig. S29).

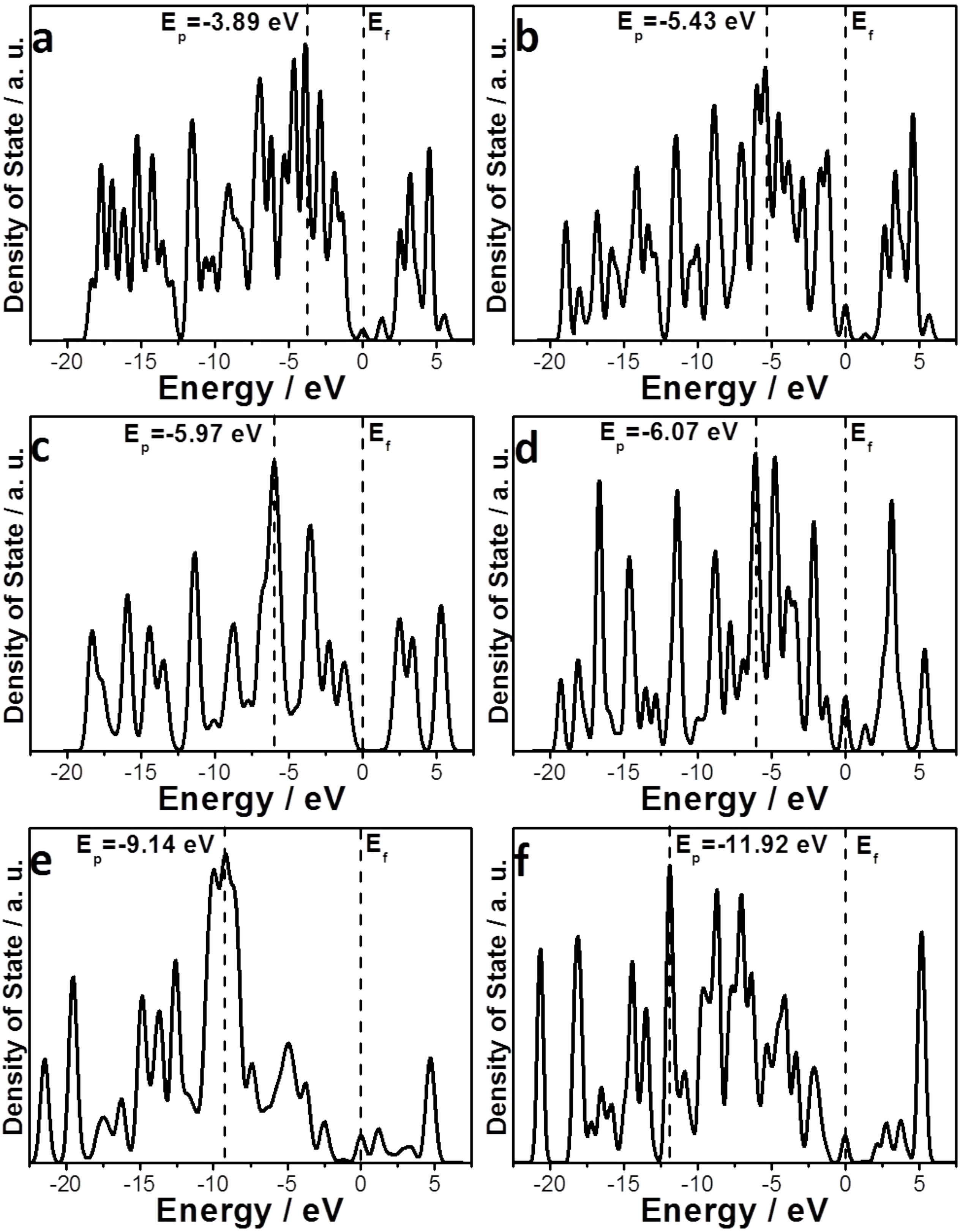

Fig. S29 DOSs of active carbon from (a) pyN, F-G, (b) gN, F-G, (c) pyN-G, (d) gN-G, (e) F-G and (f) G with OOH adsorption.

Notes and references

S1. B. Delley, *J. Chem. Phys.*, 1990, **92**, 508-517.

S2. B. Delley, *J. Chem. Phys.*, 2000, **113**, 7756-7764.

S3. H. J. Monkhorst, *Phys. Rev. B*, 1976, **13**, 5188--5192.

S4. I. C. Man, H.-Y. Su, F. Calle-Vallejo, H. A. Hansen, J. I. Martínez, N. G. Inoglu, J. Kitchin, T. F. Jaramillo, J. K. Nørskov and J. Rossmeisl, *ChemCatChem*, 2011, **3**, 1159-1165.

S5. J. K. Nørskov, J. Rossmeisl, A. Logadottir, L. Lindqvist, J. R. Kitchin, T. Bligaard and H. Jónsson, *J. Phys. Chem. B*, 2004, **108**, 17886-17892.

S6. Y. Jia, L. Zhang, A. Du, G. Gao, J. Chen, X. Yan, C. L. Brown and X. Yao, *Adv. Mater.*, 2016.

S7. W. Sheng, M. N. Myint, J. G. Chen and Y. Yan, *Energy Environ. Sci.*, 2013, **6**, 1509-1512.

S8. Y. G. Andreev and P. G. Bruce, *J. Appl. Crystallogr.*, 2016, **49**.

S9. Y. Ito, W. Cong, T. Fujita, Z. Tang and M. Chen, *Angew. Chem.*, 2015, **54**, 2131-2136.

S10. H. Guo and Q. Gao, *Int. J. Hydrogen Energy*, 2010, **35**, 7547-7554.

S11. T. Horikawa, N. Sakao, T. Sekida, J. I. Hayashi, D. D. Do and M. Katoh, *Carbon*, 2012, **50**, 1833-1842.

S12. J. In‐Yup, M. J. Ju, J. Xu, C. Hyun‐Jung, S. Jeong‐Min, K. Min‐Jung, C. I. Taek, K. H. Mo, K. J. Cheon and L. Jae‐Joon, *Adv. Funct.l Mater.*, 2015, **25**, 1170-1179.

S13. L. Qin, R. Ding, H. Wang, J. Wu, C. Wang, C. Zhang, Y. Xu, L. Wang and B. Lv, *Nano Res.*, 2017, **10**, 305-319.

S14 R. Ma, Y. Ma, Y. Donga and J.-M. Lee, *Nano Adv.*, 2016, **1**, 50-61.

S15. R. K. Sharma and Z. Lei, *Electrochim. Acta*, 2009, **54**, 7148-7155.

S16 J. T. Robinson, J. S. Burgess, C. E. Junkermeier, S. C. Badescu, T. L. Reinecke, F. K. Perkins, M. K. Zalalutdniov, J. W. Baldwin, J. C. Culbertson and P. E. Sheehan, *Nano Lett.*, 2010, **10**, 3001-3005.

S17. W. F. Chen, C. H. Wang, K. Sasaki, N. Marinkovic, W. Xu, J. T. Muckerman, Y. Zhu and R. R. Adzic, *Energy Environ. Sci.*, 2013, **6**, 943-951.

S18. L. M. Peter, *J.f Solid State Electrochem.*, 2013, **17**, 315-326.

S19. I. Abidat, N. Bouchenafa-Saib, A. Habrioux, C. Comminges, C. Canaff, J. Rousseau, T. Napporn, D. Dambournet, O. Borkiewicz and K. Kokoh, *J. Mater. Chem. A*, 2015, **3**, 17433-17444.

S20. X. Wang, Y. V. Kolen'Ko, X. Q. Bao, K. Kovnir and L. Liu, *Angew. Chem. Int.Ed.*, 2015, **54**, 8188-8192.

S21. W. F. Chen, K. Sasaki, C. Ma, A. I. Frenkel, N. Marinkovic, J. T. Muckerman, Y. Zhu and R. R. Adzic, *Angew. Chem. Int. Ed.*, 2012, **51**, 6235–6239.

S22. T. F. Jaramillo, K. P. Jørgensen, J. Bonde, J. H. Nielsen, S. Horch and I. Chorkendorff, *Science*, 2007, **317**, 100-102.

S23 K. Gong, F. Du, Z. Xia, M. Durstock and L. Dai, *Science*, 2009, **323**, 760-764.

S24 D. Guo, R. Shibuya, C. Akiba, S. Saji, T. Kondo and J. Nakamura, *Science*, 2016, **351**, 361.

S25 J. Zhang and L. Dai, *Angew. Chem.*, 2016, **128**, 13490-13494.

S26 Y. Xu, M. Kraft and R. Xu, *Chem. Soc. Rev.*, 2016, **45**, 3039-3052.

S27 K. Qu, Y. Zheng, Y. Jiao, X. Zhang, S. Dai and S.-Z. Qiao, *Adv. Energy Mater.*, 2016, 1602068, DOI: 10.1002/aenm.201602068.

S28. Z. Yan, N. Gan, D. Wang, Y. Cao, M. Chen, T. Li and Y. Chen, *Angew. Chem. Int. Ed.*, 2015, **54**, 718-724.

S29. A. Zitolo, V. Goellner, V. Armel, M. T. Sougrati, T. Mineva, L. Stievano, E. Fonda and F. Jaouen, *Nat. Mater.*, 2015, **14**, 2659-2660.

S30. A. C. Ferrari and D. M. Basko, *Nat. Nanotechnol.*, 2013, **8**, 235-246.